

THE *SPITZER*-HETDEX EXPLORATORY LARGE AREA SURVEY II: DARK ENERGY CAMERA AND *SPITZER*/IRAC MULTIWAVELENGTH CATALOGISAK G. B. WOLD^{1,2}, LALITWADEE KAWINWANICHAKIJ^{3,4,5}, MATTHEW L. STEVANS¹, STEVEN L. FINKELSTEIN¹, CASEY PAPOVICH^{3,4}, YASWANT DEVARAKONDA¹, ROBIN CIARDULLO^{6,7}, JOHN FELDMEIER⁸, JONATHAN FLOREZ¹, ERIC GAWISER⁹, CARYL GRONWALL^{6,7}, SHARDHA JOGEE¹, JENNIFER L. MARSHALL³, SYDNEY SHERMAN¹, HEATH V. SHIPLEY¹⁰, RACHEL S. SOMERVILLE^{9,11}, FRANCISCO VALDES¹², AND GREGORY R. ZEIMANN¹³*Draft version December 13, 2018*

ABSTRACT

We present the *ugriz*-band Dark Energy Camera (DECam) plus 3.6 and 4.5 μm IRAC catalogs for the *Spitzer*/HETDEX Exploratory Large-Area (SHELA) survey. SHELA covers $\sim 24 \text{ deg}^2$ of the Sloan Digital Sky Survey (SDSS) “Stripe 82” region, with seven bandpasses spanning a wavelength range of 0.35 to 4.5 μm . SHELA falls within the footprint of the Hobby-Eberly Telescope Dark Energy Experiment (HETDEX), which will provide spectroscopic redshifts for $\sim 200,000 \text{ Ly}\alpha$ emitters at $1.9 < z < 3.5$ and also for $\sim 200,000 \text{ [OII]}$ emitters at $z < 0.5$. SHELA’s deep, wide-area multiwavelength images combined with HETDEX’s spectroscopic information, will facilitate many extragalactic studies, including measuring the evolution of galaxy stellar mass, halo mass, and environment from $1.5 < z < 3.5$. Here we present *riz*-band selected *ugriz*-band DECam catalogs that reach a 5σ depth of ~ 24.5 AB mag (for point sources with an aperture that encloses 70% of the total flux) and cover 17.5 deg^2 of the overall SHELA field. We validate our DECam catalog by comparison to the DECam Legacy Survey (DECaLS) DR5 and the Dark Energy Survey (DES) DR1. We perform IRAC forced photometry with *The Tractor* image modeling code to measure 3.6 and 4.5 μm fluxes for all objects within our DECam catalog. We demonstrate the utility of our catalog by computing galaxy number counts and estimating photometric redshifts. Our photometric redshifts recover the available $\langle z \rangle = 0.33$ SDSS spectroscopic redshifts with a 1σ scatter in $\Delta z/(1+z)$ of 0.04.

Subject headings: catalogs cosmology: observations galaxies: photometry surveys

1. INTRODUCTION

SHELA is a wide-field ($\sim 24 \text{ deg}^2$) multiwavelength survey designed to study the intrinsic and environmental processes that govern the evolution of stellar mass in galaxies from $1.5 < z < 3.5$. The survey’s large area is needed to provide statistically meaningful samples and to mitigate cosmic variance. In the following, we explain SHELA’s multi-wavelength strategy with an emphasis

on the role played by the Dark Energy Camera (DECam, Honscheid et al. 2008; Flaugher et al. 2015) imaging. The genesis and motivation of the SHELA survey has been thoroughly discussed in our paper presenting the SHELA *Spitzer* imaging (Papovich et al. 2016, P16 hereafter).

SHELA’s deep *Spitzer*/IRAC (P16) and Mayall 4m/NEWFIRM *K*-band images (Stevans et al. 2018, in prep) plus archival VICS82 survey *JK*-band images (Geach et al. 2017) will provide accurate stellar mass measurements for $M \gtrsim 2 \times 10^{10} M_\odot$ galaxies with known $1.5 < z < 3.5$ redshifts. While HETDEX (Hill et al. 2008) will provide spectroscopic redshifts for an important calibrating sample, the vast majority ($\sim 70\%$) of the IRAC selected galaxies from $1.5 < z < 3.5$ will lack HETDEX detectable emission lines resulting in poorly constrained spectroscopic redshifts. Thus, deep optical imaging combined with our redder bandpasses are needed to measure photometric redshifts as well as probe the rest-frame ultraviolet.

To meet this requirement, we utilize DECam’s wide field of view (3 deg^2) to obtain deep *ugriz*-band images covering 17.5 deg^2 of the overall SHELA field. We note that our field is contained within the DECam Legacy Survey (DECaLS¹⁴) which is a *grz*-band DECam survey covering 6700 deg^2 of the equatorial sky. Although the nominal depth of DECaLS is ~ 1 magnitude shallower than our images, this collaboration plans to incorporate all publicly available

¹ Department of Astronomy, The University of Texas at Austin, 2515 Speedway, Stop C1400, Austin, Texas 78712, USA

² NASA Goddard Space Flight Center, Greenbelt, MD, 20771, USA; isak.g.wold@nasa.gov

³ Department of Physics and Astronomy, Texas A&M University, College Station, TX, 77843, USA

⁴ George P. and Cynthia Woods Mitchell Institute for Fundamental Physics and Astronomy, Texas A&M University, College Station, TX, 77843, USA

⁵ LSSTC Data Science Fellow

⁶ Department of Astronomy & Astrophysics, The Pennsylvania State University, University Park, PA 16802, USA

⁷ Institute for Gravitation and the Cosmos, The Pennsylvania State University, University Park, PA 16802, USA

⁸ Department of Physics and Astronomy, Youngstown State University, Youngstown, OH 44555, USA

⁹ Department of Physics and Astronomy, Rutgers, The State University of New Jersey, 136 Frelinghuysen Rd, Piscataway, NJ 08854, USA

¹⁰ Department of Physics & Astronomy, Tufts University, 574 Boston Avenue Suites 304, Medford, MA 02155, USA

¹¹ Center for Computational Astrophysics, Flatiron Institute, 162 5th Ave, New York, NY 10010, USA

¹² National Optical Astronomy Observatories, P.O. Box 26732, Tucson, AZ 85719, USA

¹³ Hobby Eberly Telescope, University of Texas, Austin, TX, 78712, USA

¹⁴ <http://legacysurvey.org/>

DECam datasets - including equatorial Dark Energy Survey (DES, [Dark Energy Survey Collaboration et al. 2016](#); [Abbott et al. 2018](#)) DECam data and our SHELA DECam data. Thus, we expect our *grz*-band DECam catalog depth to be comparable to DECaLS, and we explore this topic in Section 3.7. We emphasize that DECaLS does not include *i*-band data and – critical to our photometric measurements – does not include *u*-band data.

We need deep *u*-band imaging to accurately select $z > 1.5$ galaxies via their Lyman-break. Our SHELA *u*-band images are 1.5 mag deeper than the existing SDSS Stripe 82 *u*-band data which has a 5σ depth of ~ 23.9 AB mag. The importance of *u*-band imaging to accurately measure photometric redshifts between $2 \lesssim z \lesssim 3.5$ is well known and has been discussed by many previous studies (e.g., [Brunner et al. 1997](#); [Brammer et al. 2008](#)). As a proof of concept, in Section 5.1 we compare our SHELA *ugriz*+*JK*+IRAC photometric redshifts to the available $z < 2$ SDSS spectroscopic data and show that we accurately recover spectroscopic redshifts with a 1σ scatter in $\Delta z/(1+z)$ of 0.04.

Rather than simply cross-matching our DECam catalog to the existing SHELA IRAC catalog ([P16](#)), we perform forced photometry with *The Tractor* image modeling code to measure 3.6 and 4.5 μ m fluxes for all objects within our DECam catalog. This allows us to detect extremely faint sources that fall well below the 5σ depth threshold of the original SHELA IRAC catalog (22 AB mag [P16](#)). Additionally, the improved DECam resolution allows us to accurately measure fluxes for blended IRAC sources.

In the following sections we discuss the DECam data reduction, photometric depth estimates, construction of the catalog, computation of number counts, and IRAC forced photometry. Unless otherwise noted, we give all magnitudes in the AB magnitude system ($m_{AB} = 23.9 - 2.5 \log_{10} f_\nu$ with f_ν in units of μ Jy).

2. OBSERVATIONS

We observed with the Blanco 4-m telescope at CTIO using the 3 deg² DECam imager and the *u*, *g*, *r*, *i*, and *z*-band filters. DECam is a prime focus optical imager that has a focal plane array consisting of sixty-two 2K×4K pixel CCDs. Data were obtained over 5 nights in the 2013B semester (PI: Papovich; NOAO PID: 2013B-0438), with one of these nights lost due to weather. As shown in Figure 1, we observed six slightly overlapping pointings covering a total area of 17.5 deg².

We supplement our data with overlapping DES data. DES DR1 is a DECam survey that images ~ 5000 square degrees in the *grizY*-bands to a 10σ depths of [*grizY*] $\sim [24.3, 24.1, 23.4, 22.7, 21.4]$ AB mag ([Abbott et al. 2018](#)). The majority of DES lies at $\delta < -25$, but it has an extension to cover Stripe 82 and our SHELA field. For the catalog presented in this paper, we incorporate all the non-proprietary DES *griz*-band images observed prior to October 2014 within the footprint of our SHELA field. These DES images are also included in Figure 1 but are restricted to the footprint of our DECam survey. We also use Figure 1 to show the total exposure time in each tile and bandpass (also see Section 3.6 for the area and median exposure time of each tile).

3. DATA REDUCTION

We obtained all the non-proprietary NOAO Community Pipeline (CP; see the NOAO Data Handbook¹⁵) reduced DECam *ugriz* mosaics and associated data quality maps (DQMs) observed prior to October 2014 within the SHELA survey area from the NOAO Science Archive. This consisted of data from both our SHELA DECam survey and the DES. For each band, we stacked the available data into four 2.8125 by 2.68125 degree tiles, designated B3, B4, B5, and B6. By design, each tile overlaps with its neighboring tile by approximately 1 arc-minute. In this paper, we present the DECam data over the region that has imaging in all 5 *ugriz*-bands. In Figure 1, we show the field of view of our DECam images and our tiling strategy.

3.1. Image Stacking

Our DECam data stacking procedure began with the NOAO DECam CP resampled images. The NOAO DECam CP resampled images have been photometrically and astrometrically calibrated with pixels aligned to a common 0.27 arcsec/pixel grid (see the NOAO Data Handbook¹⁵ for details). The NOAO CP is an automated image reduction pipeline incorporating algorithms and elements from DES, IRAF, and earlier NOAO pipelines. The accuracy of the astrometry is limited by the science exposure depth and the accuracy and overlap with the calibrating catalog, which is currently the 2MASS catalog. The NOAO CP photometric calibration uses the USNO-B1 catalog as the photometric reference and is not adequate for science according to the NOAO Data Handbook.

For these reasons, we recalibrate these resampled images to more closely match the photometry and astrometry of SDSS. For each science image, we first generate an initial SExtractor (SE; [Bertin & Arnouts 1996](#)) catalog. We use this catalog to determine the relative astrometry and to determine the relative flux scaling factors required to adjust all images to a common flux scale. We determine the relative astrometry by computing the x- and y-offset required to match SDSS coordinates for ‘good’ stars. We define ‘good’ stars as SDSS classified stars (class=6) with a SDSS signal to noise ratio greater than 10 and no internal or external SExtractor flags in our initial catalog. The typical offset we applied was ~ 100 mas (with a measured 1σ scatter of ~ 150 mas), which is within the quoted NOAO CP accuracy of ~ 200 mas.

To determine the relative flux scaling factors, we must first measure the total fluxes for isolated PSF stars. We define isolated PSF stars as ‘good’ stars with no neighbors within 5 arc-seconds in our initial catalog. From these isolated point sources, we determine the aperture that on median encloses 70% of the 5 arc-second aperture flux. We chose a 5 arc-second aperture diameter to mitigate flux contribution from neighboring sources. This 70% aperture flux is divided by a 0.7 correction factor to obtain the total flux measurements. With total flux measurements for each exposure, we determine the relative scaling factors required to scale all images to a designated reference image. For each band, the reference image was selected from tile B5 and at least 1,500

¹⁵ <http://ast.noao.edu/data/docs>

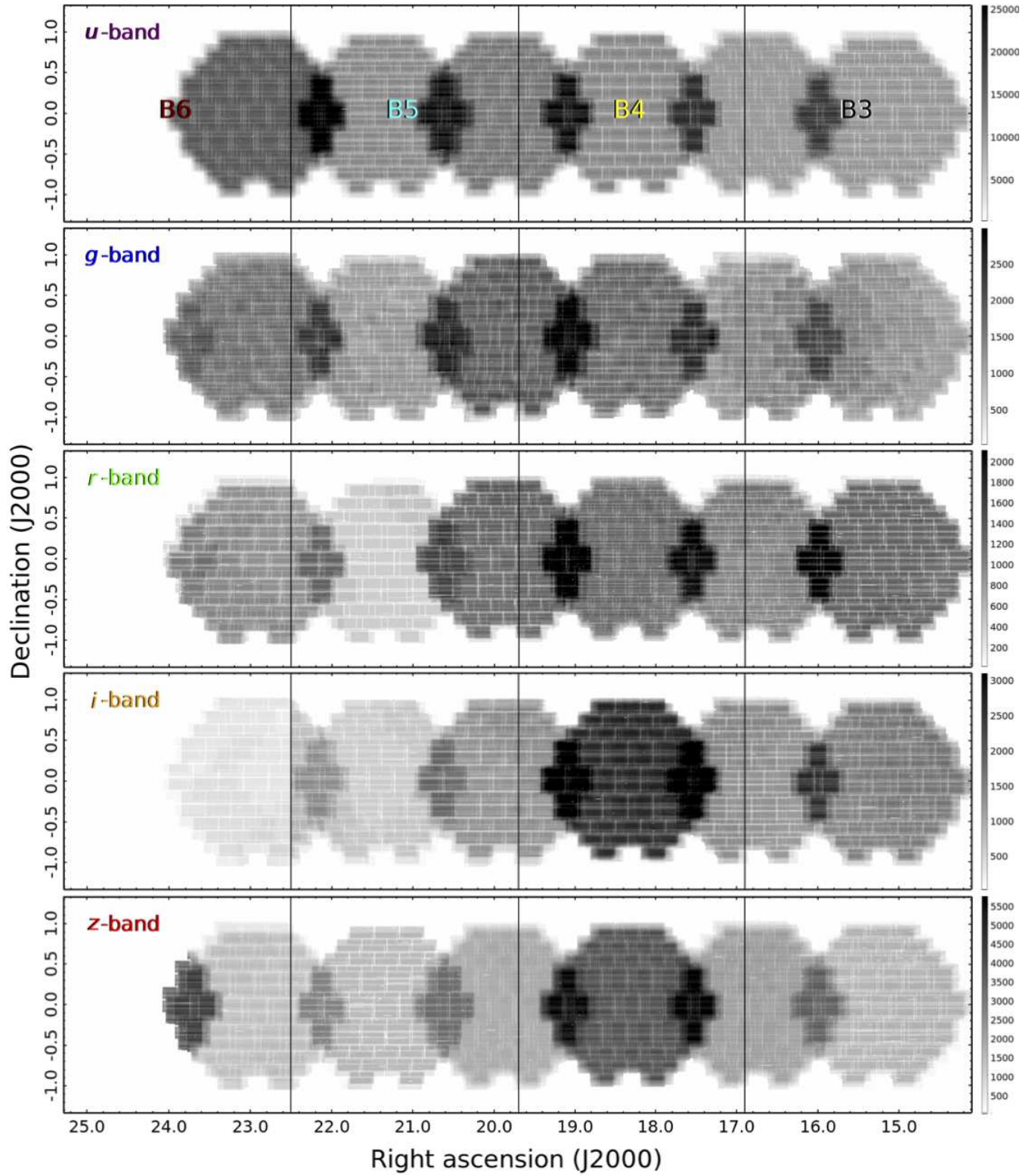


FIG. 1.— SHELA *ugriz*-band exposure maps demonstrating the survey's relative depth and area. The maps are divided into our four 2.8125 by 2.68125 degree tiles (B3, B4, B5, and B6; see top *u*-band panel). Right ascension and declination are shown in degrees. The shaded vertical bars display the exposure time in seconds. Our survey combines the *ugriz*-band DECam SHELA images with the overlapping *griz*-band DES images observed prior to October 2014.

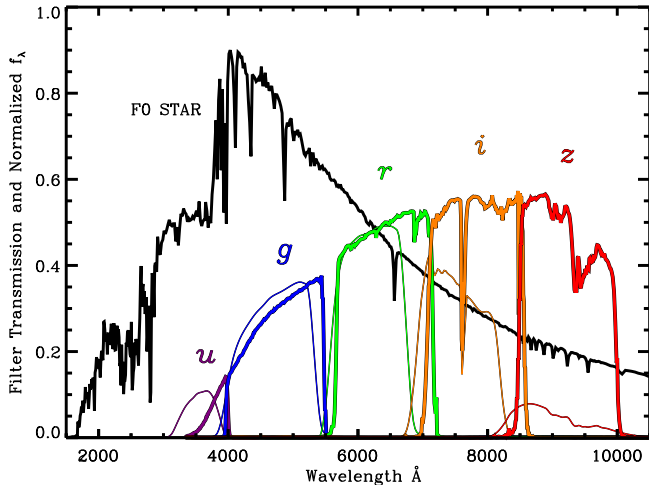


FIG. 2.— Total system throughput for DECam filters (thick curves) and SDSS filters (thin curves) and a normalized F0 star spectrum.

PSF stars were identified. The flux scaling factors were typically centered at unity with a standard deviation of ~ 0.1 .

We offset astrometry of each exposure to match SDSS and make an initial photometrically scaled stack with SWarp (Bertin et al. 2002). We remove any exposure with measured seeing worse than 2.5 arc-seconds from the stack ($\sim 2\%$ of the exposures meet this criteria). We also remove a small number of images with obvious distortions or other severe artifacts. This initial stack is weighted by:

$$w_i^{SB} = \left(\frac{1}{p_i \text{rms}_i} \right)^2 \quad (1)$$

where p_i is the flux scaling factor and rms_i is the pixel-by-pixel rms measured from background pixels in the science image. This weighting scheme is the surface-brightness-optimized weighting discussed in detail by Gawiser et al. (2006). Any region assigned a non-zero DQM value is given a weight of zero with one exception. We found that the NOAO CP multi-exposure transient flagging procedure occasionally fails and incorrectly flags the cores of bright stars. To mitigate this problem we ignore all multi-exposure transient flags that overlap with bright SDSS stars. We use the recommended Lanczos3 SWarp resampling which preserves signal, while producing only modest artifacts around image borders.

With this initial stacked image, we determined the typical seeing, $\text{FWHM}_{\text{target}}$, and a seeing upper limit, FWHM_{up} . The $\text{FWHM}_{\text{target}}$ and FWHM_{up} are used to equalize the stacked point spread function. Images with seeing less than $\text{FWHM}_{\text{target}}$ are Gaussian smoothed to achieve this target FWHM value. Images with seeing greater than FWHM_{up} are excluded from the final stack. We note that our PSF equalization procedure is very similar to the method used by SDFRED, the standard Subaru Suprime-Cam reduction package (Ouchi et al. 2004). The main advantage of this procedure is that it allows us to achieve a uniform PSF without smoothing to the largest PSF size. Three members of our team independently optimized the $\text{FWHM}_{\text{target}}$ and the FWHM_{up} parameters to obtain a uniform PSF (isolated PSF stars

TABLE 1
PHOTOMETRIC CALIBRATION

Filter	F0 Δm_{FILTER}	$\alpha(\text{SDSS AB color})$
<i>u</i>	0.329	...
<i>g</i>	0.022	$0.122(g - r)$
<i>r</i>	-0.002	$0.150(r - i)$
<i>i</i>	-0.021	$0.303(i - z)$
<i>z</i>	-0.009	$0.073(i - z)$

NOTE. — F0 Δm_{FILTER} is the magnitude offset between SDSS and DECam filters for an F0 star. The α parameter is the color slope required to convert AB DECam magnitudes to SDSS magnitudes.

typically have FWHMs that vary by $1\sigma \lesssim 0''.05$). Our final reductions use the PSF parameters that achieved the best found image depth. In practice the FWHM_{up} threshold was only needed and utilized on 8 of the 20 tile images.

The final stack is weighted by the point-source-optimized weighting employed by Gawiser et al. (2006):

$$w_i^{PS} = \left(\frac{s_i}{p_i \text{rms}_i} \right)^2 \quad (2)$$

where s_i is the seeing factor defined as:

$$s_i = 1 - \exp \left(-1.3 \frac{\text{FWHM}_{\text{target}}^2}{\text{FWHM}_i^2} \right) \quad (3)$$

and FWHM_i is the median FWHM measured for exposure i . This stacking procedure results in 20 (4 tiles times 5 bandpasses) PSF-matched science images and a corresponding number of weight maps (the sum of input weights, w_i^{PS}). We emphasize that a target FWHM must be known prior to producing a point-source-optimized stack, and we estimate the target FWHM by first producing a surface-brightness-optimized stack.

3.2. Zero-point determination

We first derived the image zero-points using two different determinations. In the first zero-point determination method, we isolate F0 stars with a SDSS color cut. We used F0 stars as a reference because of their large number density and their relatively flat SED compared to lower-mass stars. Using SDSS filter transmission curves and a Kurucz (1993) F0 spectral energy distribution (SED), we determined the expected colors of a F0 star. Using these colors, we constructed the following color cut to achieve a large sample ($N > 200$ per tile) of F0 stars:

$$\begin{aligned} & (u_{\text{SDSS}} - g_{\text{SDSS}} - 0.96)^2 + (g_{\text{SDSS}} - r_{\text{SDSS}} - 0.14)^2 \\ & + (r_{\text{SDSS}} - i_{\text{SDSS}} + 0.03)^2 + (i_{\text{SDSS}} - z_{\text{SDSS}} + 0.09)^2 \\ & < 0.35^2 \end{aligned} \quad (4)$$

The DECam filter set is not an exact match to the SDSS filter set (see Figure 2). For this reason, we computed the expected magnitude offset between like filters (Δm_{FILTER}) assuming the available filter transmission curves and a Kurucz (1993) F0 SED. The zero-point was

then determined by:

$$ZPT_{F0} = \text{median}(m_{SDSS}^{AB} - m_{DECam} - \Delta m_{FILTER}) \quad (5)$$

We report our Δm_{FILTER} values in Table 1.

In the second zero-point determination method, we examine all isolated PSF stars and assume a linear color relation between SDSS and DECam magnitudes. For example, in the g -band we assume:

$$g_{SDSS}^{AB} = g_{DECam} + ZPT_{Lin} + \alpha(g_{SDSS} - r_{SDSS}) \quad (6)$$

For tile B3, we solved for the zero-point and the color slope, α , by solving for the best-fit line. In subsequent tiles, we fixed α to the B3 value and solved for ZPT_{Lin} . We show below that this fixed α assumption does not significantly affect our zero-point determination. In Table 1, we list the best-fit color slopes and SDSS colors used for each band. In both methods the AB magnitude for the DECam filter set is:

$$g_{DECam}^{AB} = g_{DECam} + ZPT_{F0,Lin} \quad (7)$$

Our first method relies on the accuracy of the available filter profiles and the model F0 SED, while our second method relies on there being a linear color relation between SDSS and DECam magnitudes. For all bands except the u -band (here many stellar SEDs display a sharp 4000 Å break which makes the adjacent spectral slope a poor predictor of the bluer DECam u -band flux) we find a clear linear relation. Thus, we use the F0 zero-point determination for the u -band and use the linear zero-point determination for all other bands. For $griz$ -bands, we find that the maximum $|ZPT_{F0} - ZPT_{Lin}|$ is 0.04 magnitudes (see Table 2). This provides an estimate for the systematic uncertainty of our zero-points. We note that our zero-point accuracy, as judged by $|ZPT_{F0} - ZPT_{Lin}|$, does not vary significantly from one tile to the next, and this suggests that fixing α to the best-fit B3 value does not significantly affect our zero-point determination.

We note that for AB magnitudes, sources with a flat flux density (f_ν) will have an AB color of zero. Thus, taking g -band as an example, sources with an SDSS color term, $\alpha(g_{SDSS} - r_{SDSS})$, equal to zero will have $g_{SDSS}^{AB} = g_{DECam}^{AB}$. We emphasize that our cataloged magnitudes are AB for the observed DECam filters and will in general differ from SDSS magnitudes by the SDSS color term, $\alpha(g_{SDSS} - r_{SDSS})$. For all zero-point calculations, we offset the SDSS u - and z -band magnitudes by -0.04 and -0.02 , respectively, to bring them in alignment with AB magnitudes¹⁶.

With zero-points accurately measured, we convert the image units to nJy per pixel. This convention results in final image zero-points of 31.4:

$$m_{AB} = -2.5 \log_{10} f_{nJy} + 31.4 \quad (8)$$

Our grz -band images are contained within DECaLS. DECaLS will image 6700 deg² of the SDSS/BOSS extragalactic footprint that lies in the region $-20 < \delta < +30^\circ$ to depths of approximately $g = 24.7$, $r = 23.9$, and

TABLE 2
PHOTOMETRIC COMPARISON

Tile	Filter	$ZPT_{F0} - ZPT_{Lin}$	$ZPT_{DECaLS} - ZPT_{Lin}$	$ZPT_{DES} - ZPT_{Lin}$
B3	u
	g	0.03 ± 0.08	0.02 ± 0.03	0.04 ± 0.03
	r	0.01 ± 0.07	-0.05 ± 0.05	-0.00 ± 0.04
	i	0.04 ± 0.08	...	0.03 ± 0.03
	z	0.01 ± 0.09	-0.05 ± 0.03	0.02 ± 0.03
B4	u
	g	0.03 ± 0.08	0.01 ± 0.03	0.03 ± 0.03
	r	0.01 ± 0.07	-0.04 ± 0.02	-0.00 ± 0.03
	i	0.04 ± 0.07	...	0.03 ± 0.02
	z	0.01 ± 0.09	-0.04 ± 0.04	0.02 ± 0.04
B5	u
	g	0.03 ± 0.08	0.01 ± 0.03	0.03 ± 0.03
	r	0.01 ± 0.06	-0.04 ± 0.02	-0.01 ± 0.03
	i	0.04 ± 0.09	...	0.04 ± 0.04
	z	0.01 ± 0.09	-0.05 ± 0.03	0.02 ± 0.02
B6	u
	g	0.03 ± 0.08	0.01 ± 0.02	0.03 ± 0.03
	r	0.01 ± 0.07	-0.03 ± 0.02	0.00 ± 0.02
	i	0.03 ± 0.07	...	0.03 ± 0.02
	z	0.00 ± 0.10	-0.05 ± 0.02	0.02 ± 0.02

NOTE. — $ZPT_{F0} - ZPT_{Lin}$ is the median zero-point offset between our F0 and our linear color determination method. $ZPT_{DECaLS} - ZPT_{Lin}$ is the median zero-point offset between DECaLS and our linear color determination method. $ZPT_{DES} - ZPT_{Lin}$ is the median zero-point offset between DES and our linear color determination method. The errors indicate 1.48 times the median absolute deviation.

$z = 23.0$ AB mag (5σ point-source). This survey intends to take advantage of all non-DECaLS data that lies within their survey area. Thus, the final DECaLS data release will incorporate data from DES and our dataset and their grz -band images should have comparable depth with our images (see Section 3.7 for further discussion). Comparing their data release 5 (DR5) cataloged grz -band data to our catalog of isolated PSF stars, we find that our zero-points disagree by at most 0.05 magnitudes (see Table 2). DECaLS's DR5 zero-points are computed from Pan-Starrs PS1 photometry assuming a third order polynomial color relation between PS1 and DECam magnitudes. We find that altering our calibration reference catalog from SDSS to PS1 but keeping our linear color relation alters our computed zero-points by ~ 0.02 magnitudes. We attribute the remaining SHELAL / DECaLS zero-point offset to the different methods employed to compute the zero-points (our linear adjacent color relation vs. DECaLS' polynomial color relation). We decided to keep our linear color relation method because of its use of adjacent color terms (which should be a better measure of the local spectral slope), rather than DECaLS's convention of using a $(g-i)$ color in all bands.

Recently, DES has published DR1 (Abbott et al. 2018) with a reported photometric precision of $< 1\%$ in all bands. Comparing their DR1 cataloged $griz$ -band data to our catalog of isolated PSF stars, we find that our zero-points disagree by at most 0.04 magnitudes (see Table 2). Both DES and DECaLS suggest that our g -band zeropoint is systematically offset by $\sim 3\%$. However, DES agrees with our r and z -band zeropoints ($\leq 2\%$), while DECaLS suggests a $\sim 4\%$ correction. Given these issues, we leave our zeropoints unchanged and adopt a 5% systematic uncertainty in our cataloged flux errors (See Section 3.6).

¹⁶ <http://classic.sdss.org/dr7/algorithms/fluxcal.html>

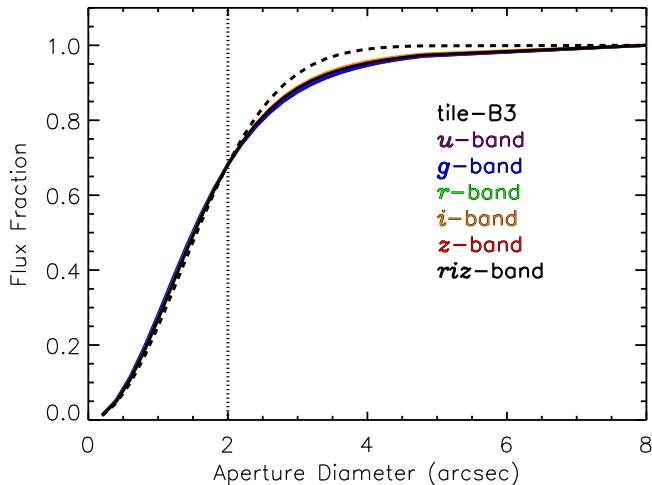


FIG. 3.— Median curve of growth for isolated stars in the PSF-matched B3 tile. We show curves of growth for our *ugriz*-band and for our detection *riz*-band image. For comparison, we also show a Gaussian profile with the dashed black curve. The dotted vertical line indicates the 70% flux aperture used to compute the total flux for point sources. For our completeness simulations, we insert fake Gaussian sources (profile shown by dashed black curve) with FWHM set to match the measured 70% curve of growth flux fraction. (The complete figure set (4 images) for all SHELTA tiles is available in the online journal.)

3.3. Final PSF Matching

For each tile, we degrade the PSF to match the measured PSF in the bandpass with the worst seeing. We perform this final Gaussian PSF matching to ensure that an aperture with fixed size will enclose the same fraction of a point-source’s flux regardless of the observed bandpass. In particular, we wish to scale up a fixed 70% aperture flux to determine the total flux of point sources. In Figure 3, we show the median fraction of flux enclosed vs. aperture diameter for isolated stars in the B3 tile. In Table 3, we report the half-light diameter for isolated stars before and after final PSF matching for all bandpasses and tiles. In Table 3, we also report the our adopted 70% aperture diameter and the precise amount of flux enclosed within this aperture. We have adopted the convention of sampling aperture diameters every $0''.2$, thus the closest PSF aperture will enclose slightly more or less flux than 70%. The cataloged total fluxes are adjusted accordingly. For example, we compute the total AB *u*-band magnitude in tile B3 via:

$$u_{AB}^{tot} = u_{AB}^{2''0} + 2.5 \log_{10} 0.68 \quad (9)$$

We emphasize that our total PSF fluxes are only accurate for point sources. For resolved objects, we catalog SExtractor MAG_AUTO magnitudes. SExtractor’s AUTO aperture uses a Kron ellipse adjusted to each object’s light profile and is meant to give the most precise SExtractor estimate of total magnitude.

3.4. Detection Image and Source Extraction

For each tile, we compute an inverse variance-weighted summation of the *r*, *i*, and *z*-bands to construct a detection image. The variance image is formed by normalizing our inverse weight maps (described in Section 3.1) to the variance measured in our science frames prior to final PSF matching. For each tile all images were scaled to

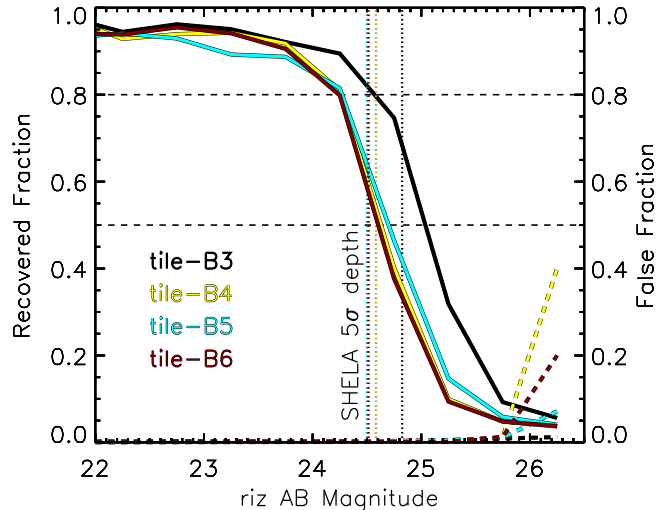


FIG. 4.— Recovered fraction as a function of input *riz*-magnitude for simulated point sources. We added simulated point sources with no color ($u = g = r = i = z$) to all of the science images and then employed our normal source extraction procedure. The solid red, orange, green, and blue curves indicate the recovered fraction of simulated sources for tiles B3, B4, B5, and B6, respectively. The dashed curves indicate the estimated false detection fraction as a function of magnitude. We inverted the detection image and measured the number of negative sources extracted per magnitude bin. We took the ratio of the number of negative sources to the number of sources extracted from our science images to estimate false detection fraction. We find a 50% (80%) completeness limit at ~ 24.7 (~ 24.4) mag. False sources only become significant at magnitudes fainter than our estimated 10% completeness limit. We indicate our catalog’s 5σ depth with vertical dotted lines, see Section 3.6 for details.

a common nJy scale and have approximately the same PSF. Thus, our inverse variance weighting is consistent with the point-source optimized weighting employed by Gawiser et al. (2006). We decided not to use the *u* and *g*-bands in our detection image because many high-redshift ($z > 3.5$) galaxies will dropout of these bands, so their inclusion would only add noise for these sources.

In Figure 3, we compare the detection image’s PSF (black solid curve) to the PSF in other bandpasses (purple, blue, green, orange, and red curves) using tile B3 as an example. As expected the agreement is good, and in Table 3, we quantify this agreement by showing that the same flux fraction is enclosed within our adopted PSF aperture for both our detection image and our *ugriz*-bandpass images.

We used SExtractor in double-image mode to detect and measure sources with the SExtractor parameters listed in Table 4. In this mode the first image specified is used for the detection of sources and the second image is used for measuring source properties. This allowed us to produce uniform *riz*-selected *ugriz*-band catalogs. We utilize DQMs that have non-zero pixels when all pre-stacked pixels are flagged in the NOAO CP DQMs. We also assign non-zero DQM values to regions around bright stars. Bright stars effectively mask out regions of the sky and have associated false sources that are due to diffraction spikes and saturation effects. We mitigate these issues by masking out all UCAC4 sources (Zacharias et al. 2013) with magnitudes less than 16.5. We determined a magnitude dependent circular

TABLE 3
SEEING, APERTURES, AND POINT SOURCE DETECTION LIMITS.

Tile	Filter	Input $2 \times r_{1/2}^{SE}$ Median (arcsec)	Output $2 \times r_{1/2}^{SE}$ Median (arcsec)	PSF Aperture (arcsec)	Flux Enclosed (Fractional)	Sky Aperture Detection Limit (5σ , AB)	Simulation Detection Limit (5σ , AB)	DECaLS DR5 Detection Limit (5σ , AB)
B3	<i>u</i>	1.38	1.48	2.0	0.68	25.4	25.1	...
	<i>g</i>	1.47	1.47	2.0	0.68	25.1	24.9	25.2
	<i>r</i>	1.37	1.49	2.0	0.68	24.8	24.7	24.9
	<i>i</i>	1.18	1.50	2.0	0.68	24.3	24.1	...
	<i>z</i>	1.14	1.49	2.0	0.68	23.9	23.6	23.8
	<i>riz</i>	...	1.49	2.0	0.68	25.0	24.8	...
B4	<i>u</i>	1.41	1.59	2.2	0.71	25.4	24.9	...
	<i>g</i>	1.54	1.54	2.2	0.71	25.1	24.8	25.1
	<i>r</i>	1.34	1.58	2.2	0.71	24.7	24.5	24.9
	<i>i</i>	1.15	1.59	2.2	0.71	24.2	24.0	...
	<i>z</i>	1.42	1.56	2.2	0.71	23.7	23.5	23.8
	<i>riz</i>	...	1.57	2.2	0.71	24.7	24.6	...
B5	<i>u</i>	1.43	1.56	2.2	0.71	25.4	25.0	...
	<i>g</i>	1.54	1.54	2.2	0.71	25.0	24.8	25.2
	<i>r</i>	1.34	1.58	2.2	0.71	24.4	24.3	24.7
	<i>i</i>	1.26	1.58	2.2	0.71	23.8	23.5	...
	<i>z</i>	1.21	1.59	2.2	0.71	23.7	23.5	23.5
	<i>riz</i>	...	1.59	2.2	0.71	24.6	24.5	...
B6	<i>u</i>	1.52	1.54	2.2	0.71	25.3	24.9	...
	<i>g</i>	1.53	1.53	2.2	0.71	25.0	24.8	25.1
	<i>r</i>	1.37	1.55	2.2	0.71	24.5	24.4	24.8
	<i>i</i>	1.31	1.57	2.2	0.71	23.7	23.4	...
	<i>z</i>	1.23	1.58	2.2	0.71	23.6	23.4	23.8
	<i>riz</i>	...	1.56	2.2	0.71	24.6	24.5	...

NOTE. — The half-light radius ($r_{1/2}^{SE}$) is the radius containing 50% of the total light, where the total light is measured within SExtractor’s AUTO aperture. Twice the half-light radius is the half-light diameter, which is a robust estimate of the seeing FWHM (e.g., [Gawiser et al. 2006](#)). As described in Section 3.3, the ‘PSF Aperture’ column shows the circular aperture diameter that contains approximately 70% of the total light for points sources, where the total light is measured by a $8''$ aperture diameter. The ‘Flux Enclosed’ column shows the precise amount of flux enclosed within our PSF aperture. The tabulated sky aperture and simulation 5σ detection limits are described in Section 3.6 and illustrated in Figure 6. The DECaLS DR5 detection limits are described in Section 3.7.

TABLE 4
SHELA SExtractor PARAMETER SETTINGS

SExtractor Parameter	Value
DETECT_MINAREA	3 pixels
DETECT_THRESH	1.5
ANALYSIS_THRESH	1.5
FILTER_NAME	Gauss_3.0_7x7.conv
WEIGHT_TYPE	MAP_RMS,MAP_RMS
DEBLEND_NTHRESH	32
DEBLEND_MINCONT	10^{-5}
MAG_ZEROPOINT	31.4
PIXEL_SCALE	0.27 arcsec
BACK_TYPE	AUTO,AUTO
BACK_SIZE	256
BACK_FILTERSIZE	4
MASK_TYPE	CORRECT
CLEAN	NO

star mask defined by:

$$\text{Radius} = 319.7 - 41.9R + 1.4R^2 \quad (10)$$

where the radius is in arcsec and R is the UCAC4 fit model magnitude with bandpass spanning 5790 – 6420 Å. We constructed this star mask by adjusting circular regions centered on UCAC4 stars to include all obvious false sources (e.g., sources associated with diffraction spikes) for a sample of stars with a wide range of magnitudes. With these radii and magnitudes, we fit a polynomial of degree 2, resulting in Equation 10 (for a similar

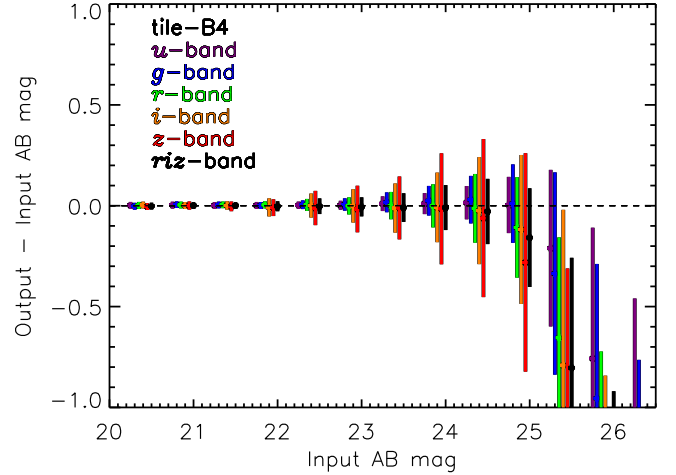


FIG. 5.— Median difference between measured output and known input magnitude of fake sources as a function of input magnitude for tile B4. The error bars indicate 1.48 times the median absolute deviation (σ_{MAD}). For clarity data points are slightly offset in the x-direction from the unaltered position occupied by the u-band data points. The median difference between the input and recovered magnitude is near zero for objects brighter than ~ 24.5 mag. We use these magnitude errors to estimate our catalog’s 5σ depth, see Section 3.6 and Figure 3. (The complete figure set (4 images) for all SHELA tiles is available in the online journal.)

procedure see [Keenan et al. 2010](#)). We record both the internal (see SExtractor User’s Manual) and DQM-based

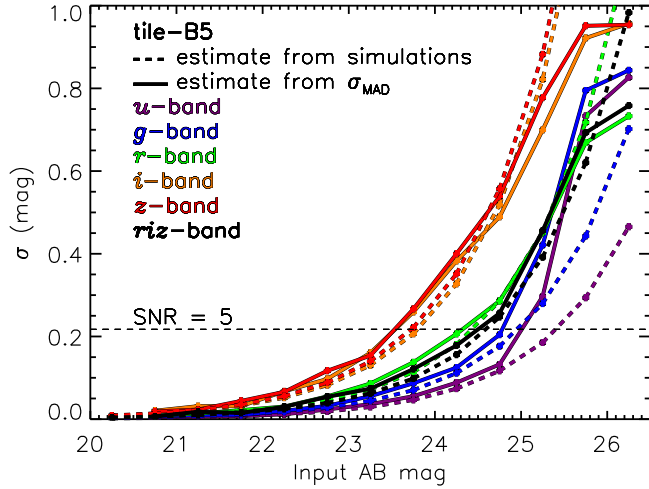


FIG. 6.— Estimated photometric uncertainties determined from our simulations (solid curves) and from the noise measured in 70% apertures scaled to total magnitudes (dashed curves) for tile B5. The black dashed line indicates the magnitude uncertainty that corresponds to a SNR= 5. The intersection of the SNR= 5 dashed line and the photometric uncertainty curves gives our catalog’s 5σ depth; recorded in Table 3 for all tiles. (The complete figure set (4 images) for all SHELA tiles is available in the online journal.)

external SExtractor flags in our final catalog.

We also record SExtractor morphological information including the semimajor axis (a), the ellipticity ($e = 1 - b/a$, where b is the semiminor axis), the position angle of the semimajor axis in degrees east from celestial north (θ), the Kron radius (r_{Kron}), and the half-light radius ($r_{1/2}$).

3.5. Completeness and Purity tests

For each tile, we inserted 10,000 fake Gaussian sources with no color ($u = g = r = i = z$) into our final science images and then attempted to recover them using our extraction procedure to estimate the completeness of our catalog. We set the FWHM of the Gaussian sources to match the enclosed flux within our PSF aperture. In Figure 3, we show (with a black dashed line) the curve of growth for our fake Gaussian sources used in the B3 tile. For each fake source, we randomly assigned an image position, and we randomly sampled source flux from a Euclidean power law distribution with a minimum flux threshold of 26.5 mag. After inserting fake sources, we remade our detection image and then performed our standard extraction procedure. We repeated this simulation 10 times resulting in 100,000 fake input sources per tile.

For a given simulation and tile, we use the same *riz*-band detection image for all bands. Thus, the number of detected fake objects and the estimated completeness does not vary with bandpass. In Figure 4, we show the recovered fraction of fake sources as a function of magnitude (solid curves). Our simulations indicate that our catalogs are 80% complete at a magnitude of ~ 24.4 . After this threshold, our completeness quickly falls off with a 50% completeness limit at ~ 24.7 mag.

We also estimate the purity of our sample by inverting all our science images (multiplying all pixels values by -1), forming an inverted detection image, and then performing our standard extraction procedure on these images. Assuming that positive noise spikes are as likely as negative noise spikes, this analysis will estimate

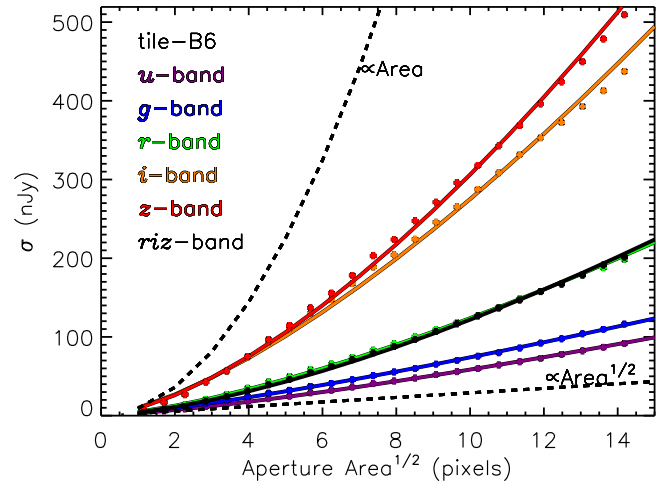


FIG. 7.— Measured aperture noise as a function of the square root of the aperture area measured in pixels for tile B6. As expected our aperture noise falls between the dashed lines which correspond to the limiting cases of uncorrelated and perfectly correlated pixels. We use these aperture noise measurements to estimate our catalog’s 5σ depth, see Section 3.6 and Figure 3. (The complete figure set (4 images) for all SHELA tiles is available in the online journal.)

TABLE 5
SURVEY AREA, EXPOSURE TIME, AND COEFFICIENTS FOR
ERROR ESTIMATES USING SKY APERTURES.

Tile	Filter	Area (deg ²)	Median t_{exp} (ks)	σ_1 (nJy)	α	β
B3	<i>u</i>	4.850	8.401	3.81	0.72	1.36
	<i>g</i>	4.856	1.159	4.38	0.88	1.31
	<i>r</i>	4.856	1.000	5.15	0.78	1.42
	<i>i</i>	4.856	1.289	9.69	0.63	1.47
	<i>z</i>	4.856	1.590	17.08	0.48	1.51
	<i>riz</i>	4.856	3.799	4.54	0.68	1.50
B4	<i>u</i>	5.145	10.798	3.63	0.54	1.44
	<i>g</i>	5.152	1.559	4.66	0.81	1.29
	<i>r</i>	5.152	1.090	7.54	0.52	1.44
	<i>i</i>	5.152	1.980	13.13	0.42	1.51
	<i>z</i>	5.152	3.090	12.71	0.81	1.42
	<i>riz</i>	5.152	6.271	5.83	0.58	1.51
B5	<i>u</i>	4.910	11.991	3.69	0.57	1.42
	<i>g</i>	4.912	1.269	4.73	0.87	1.29
	<i>r</i>	4.912	0.600	7.65	0.61	1.47
	<i>i</i>	4.912	0.690	11.58	0.73	1.47
	<i>z</i>	4.912	1.500	12.60	0.64	1.54
	<i>riz</i>	4.912	2.690	5.60	0.64	1.53
B6	<i>u</i>	2.567	14.399	3.48	0.83	1.31
	<i>g</i>	2.570	1.449	4.39	0.93	1.26
	<i>r</i>	2.570	0.780	7.19	0.65	1.42
	<i>i</i>	2.570	0.290	12.72	0.78	1.44
	<i>z</i>	2.570	1.200	18.12	0.50	1.53
	<i>riz</i>	2.570	2.378	5.95	0.65	1.50

how many false sources are extracted within our catalog. In Figure 4, we show the fraction of false sources as a function of magnitude (dashed curves). We estimate that false sources only become significant at magnitudes fainter than our estimated 10% completeness limit.

3.6. Detection Limits and Photometric Errors

Following the procedure used by P16, we estimate the photometric depth of our catalogs using two methods. The first method uses the results from our completeness simulations. In Figure 5, we show the median difference

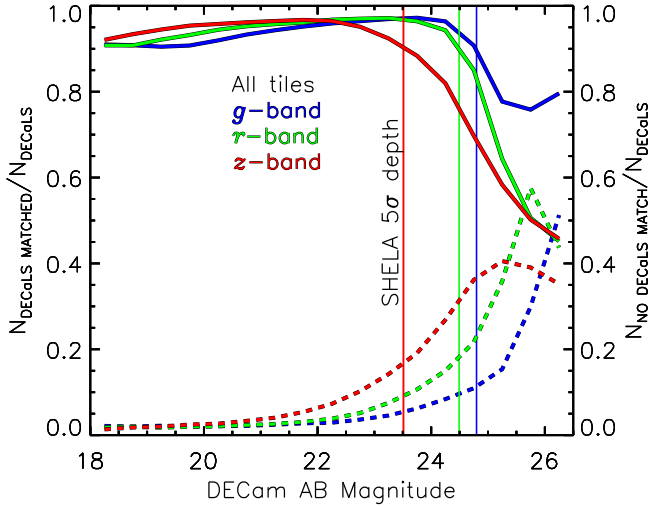


FIG. 8.— The ratio of the number of SHELA sources with DECaLS DR5 counterparts ($N_{\text{DECaLS MATCHED}}/N_{\text{DECaLS}}$) to the total number of cataloged DECaLS DR5 sources within the SHELA field (N_{DECaLS} ; solid red, green, and blue curves) and the ratio of unmatched SHELA sources ($N_{\text{NO DECaLS MATCH}}/N_{\text{DECaLS}}$) to the total number of cataloged DECaLS DR5 sources within the SHELA field (N_{DECaLS} ; dashed red, green, and blue curves) versus magnitude. We find that our catalog has a deficit of bright sources (< 21 mag) relative to DECaLS. Primarily, we attribute this to artifacts within the DECaLS DR5 catalog (see Section 3.7).

between the measured output and known input magnitude of fake sources as a function of input magnitude for tile B4. The error bars indicate 1.48 times the median absolute deviation (σ_{MAD}). A magnitude error of $\simeq 0.22$ corresponds to a SNR of 5. Using these binned σ_{MAD} values, we interpolate to estimate where $\sigma_{\text{MAD}} = 0.22$. We report these 5σ detection limits based on our simulations in Table 3. In Figure 6, we show σ_{MAD} as a function of magnitude for tile B5 (solid curves). We note that these depth estimates do not account for systematic errors, but our simulations show that the median difference between the input and recovered magnitude is near zero for objects brighter than ~ 24.5 mag (e.g., see Figure 5).

For the second photometric depth estimate, we measured the image background noise as a function of photometric aperture size. We performed aperture photometry on 10,000 randomly placed sky positions. We ensured that the apertures did not overlap and that regions containing cataloged objects were excluded using the segmentation map. We then computed σ_{MAD} for the aperture fluxes. In Figure 7, we show σ_{MAD} as a function of the square root of the aperture area for tile B6. In the limiting case of uncorrelated pixels, σ_{MAD} is proportional to the square root of the aperture area (lower dashed line). At the other extreme of perfect correlation, σ_{MAD} is proportional to the aperture area (upper dashed line). To estimate the noise in an aperture of arbitrary size, we follow the procedure of Gawiser et al. (2006) and fit our data with a function with the following form:

$$\sigma_{\text{MAD}} = \sigma_1 \alpha A^{\beta/2} \quad (11)$$

where σ_1 is the median standard deviation of un-flagged background pixels, A is the aperture area, α and β are free parameters. We report these values along with the area and median exposure time of each tile in Table 5.

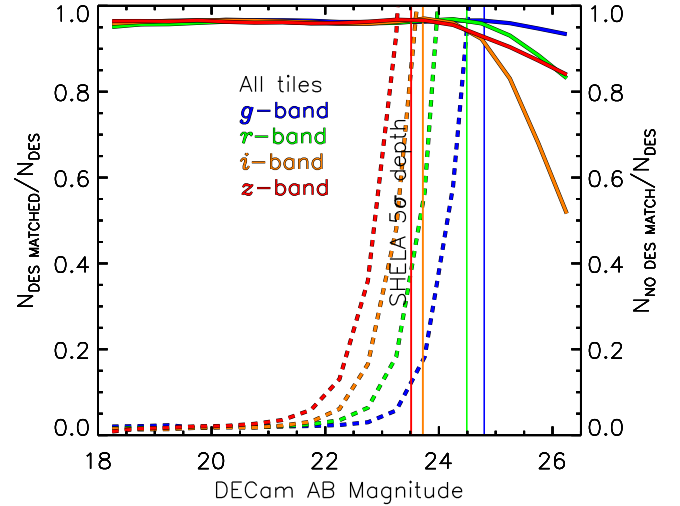


FIG. 9.— The ratio of the number of SHELA sources with DES DR1 counterparts ($N_{\text{DES MATCHED}}/N_{\text{DES}}$) to the total number of cataloged DES DR1 sources within the SHELA field (N_{DES} ; solid red, green, orange, and blue curves) and the ratio of unmatched SHELA sources ($N_{\text{NO DES MATCH}}/N_{\text{DES}}$) to the total number of cataloged DES DR1 sources within the SHELA field (N_{DES} ; dashed red, green, orange, and blue curves) versus magnitude. At bright magnitudes, we find our SExtractor-based catalog has better agreement with the SExtractor-based DES catalog relative to the Tractor-based DECaLS catalog. We attribute the upturn of unmatched SHELA sources (dashed curves) to DES DR1 incompleteness (see Section 3.7).

As expected our best fit β values fall between $\beta = 1 - 2$ indicating partially correlated pixels.

In Figure 6, we show the magnitude uncertainty computed from our B5 PSF apertures (dashed curves). We have scaled up the PSF aperture uncertainty to a total uncertainty by dividing by ~ 0.70 . We find that at bright magnitudes our two methods of estimating photometric uncertainties are within 0.02 mag (see solid and dashed curves in Figure 6). We find that our uncertainty results based on our completeness simulations are generally higher but can be brought into better agreement by ensuring that simulated sources do not overlap with real objects. Astrophysically, there is no reason to prevent sources from overlapping. Thus, we report 5σ detection limits based on our simulations (which allow overlaps) and based on measured fluctuations within sky apertures in Table 3.

For our SHELA catalog, we compute photometric errors by inputting the aperture area used to measure the object into Equation 11. For PSF apertures we increase the aperture uncertainty to a total uncertainty by dividing by a correction factor, $c_{\text{psf}} \sim 0.70$ (exact values are listed in Table 3). We add this value in quadrature with an estimated systematic uncertainty of $\sigma_{\text{sys}} = 0.05$ mag. This σ_{sys} term accounts for systematic errors in our photometric zero-points (see Section 3.2) and in the offset seen between our two methods of estimating photometric uncertainties (discussed above). Our cataloged total photometric flux error is:

$$\sigma_{\text{tot}}^2 = \left(\frac{\sigma_{\text{MAD}} \text{ rms}_i}{c_{\text{psf}} \text{ rms}_{\text{med}}} \right)^2 + \left(\frac{\ln(10) \sigma_{\text{sys}} f_i}{2.5} \right)^2 \quad (12)$$

where σ_{MAD} is computed from Equation 11, rms_{med} is the median rms for a given tile, rms_i is the rms mea-

sured at the source’s position ($c_{\text{psf}} = 1$ for MAG-AUTO apertures) and f_i is the source’s flux density.

3.7. Comparison of the SHELA Catalog to DECaLS and DES

As discussed in Section 3.2, DECaLS has independently reduced the same DECam *grz*-band data within our survey area. Consistent with our work, DECaLS DR5 calibrates photometry to the AB DECam filter system. This provides us with a direct method for verifying our *g*-, *r*-, and *z*-band catalogs. In Section 3.2, we used DECaLS to verify our zero-points. In Figure 8, we use DECaLS to estimate our catalog’s completeness and purity. By making the assumption that DECaLS is ‘truth’, we estimate the our catalog’s completeness by computing the ratio of the number of SHELA sources with DECaLS DR5 counterparts (N_{MATCHED}) to the total number of cataloged DECaLS DR5 sources within the SHELA field (N_{DECaLS}). To minimize the effects of photometric errors, we exclude all of our cataloged magnitudes with internal SExtractor flags denoting saturated, truncated, or corrupted pixels (internal SExtractor flag > 3). We also exclude magnitudes with non-zero external SExtractor flags which we use primarily to indicate the close proximity to a saturated star (see Section 3.4 for details). To ensure a fair comparison we also exclude DECaLS sources that fall within our bright star mask.

For magnitudes brighter than our $\sim 5\sigma$ detection limit, we expect $N_{\text{MATCHED}} \sim N_{\text{DECaLS}}$ indicating a $\sim 100\%$ completeness. In Figure 8, we show that the DECaLS completeness only reaches $\sim 95\%$ even for relatively bright sources ($18 < m < 21$ mag). To investigate this further, we looked for Pan-Starrs PS1 counterparts for all of the bright *g*-band DECaLS sources ($18 < m < 21$ mag) missed by our catalog. We find that $\sim 65\%$ of these sources are also missing from Pan-Starrs PS1. We randomly selected 10 DECaLS objects missed by both PS1 and our catalog and visually inspected both DECaLS and our images. These sources appear to be predominately located next to extended galaxies or saturated stars (but by our comparison setup they are all outside our bright star mask) and do not appear to be real. We estimate that $\sim 90\%$ of these sources are artifacts within the DECaLS DR5 catalog. Thus, we find no evidence that our catalog’s completeness differs significantly from our simulation estimates which indicate a $\sim 99\%$ completeness for objects with $m \leq 21$ mag.

Performing another visual spot check on the bright *g*-band objects ($18 < m < 21$ mag) contained by both PS1 and DR5 but missed by our catalog, we find that in $\sim 70\%$ of these cases our catalog counts two closely paired objects as one extended object. This is to be expected given our decision to PSF match to the bandpass with the worst seeing. Since this is estimated to affect a small percentage of sources, we make no correction to our catalog. We also note that our completeness relative to DECaLS DR5 declines to $\sim 90\%$ at our catalog’s 5σ detection limit with the most prominent decline in the *z*-band. Visually spot checking both DECaLS and our *z*-band images, we estimate that $\sim 50\%$ of these missing 5σ sources ($23 < m < 23.5$ mag) are cosmic rays contained within the DECaLS catalog. The remaining $\sim 50\%$ appear to be real sources missed by our catalog.

We also use DECaLS to estimate the impurity of our catalog. Assuming that DECaLS DR5 is ‘truth’, our catalog’s impurity is computed by taking the ratio of SHELA sources with no DECaLS counterparts ($N_{\text{NO MATCH}}$) to the total number of cataloged DECaLS sources within the SHELA field (N_{DECaLS}). Having a large percentage of unmatched objects could indicate significant artifacts in our catalog. In Figure 8, we show that our catalog’s impurity is estimated to be small ($\lesssim 5\%$) at bright magnitudes and increases to $\sim 15\%$ at our 5σ detection limit. Visually spot checking both DECaLS and our *z*-band images, we find that the majority of these $\geq 5\sigma$ objects ($m < 23.5$ mag) appear to be real in our images, but are not detected in the DECaLS DR5 images. Many of the missed objects are aligned with diffraction spikes from bright stars and it could be that DECaLS DR5 has applied a more conservative star mask in these regions.

While we have emphasized subtle differences, overall we find that DECaLS DR5 is in agreement with our catalog and appears to have a comparable depth (see Table 3). To quantify the depth of DECaLS DR5, we have selected all DR5 objects within our field of view and found the median cataloged 5σ point source depth (their ‘psfdepth’ estimate). These DR5 depths, which are based upon the formal errors in the Tractor catalogs for point sources, are roughly consistent with our SHELA depth estimates. Specifically, the depth of DECaLS DR5 is on median 0.1 mag deeper than our sky aperture depth and 0.3 mag deeper than our simulation detection limit as reported in Table 3.

In Figure 9, we replicate Figure 8 but use DES DR1 as the *griz*-band reference catalog. We find that our catalogs are in close agreement ($\pm 5\%$) over a magnitude range of $18 - 22$ AB. For fainter magnitudes the fraction of unmatched objects increases rapidly, which we interpret as DES incompleteness. We estimate that DES DR1 is 90% complete at $g = 23.5$, $r = 23.0$, $i = 22.5$, and $z = 22.2$. These estimates are within 0.3 mag of the reported DES DR1 95% completeness (Abbott et al. 2018).

3.8. Number Counts

In Figure 10, we show our *r*-band differential galaxy number counts with Poisson error bars for each SHELA tile. We identified and removed stars from our sample by cross-referencing our catalog to known SDSS stars. The reliability of SDSS star classification is expected to be robust for $r < 22$ (Lupton et al. 2001). For $r > 22$, the overall number counts are dominated by galaxies with stellar contribution estimated to be $< 10\%$. As discussed in Section 3.7, we remove cataloged sources with internal SExtractor flags > 3 and external SExtractor flags > 0 .

Our number counts agree with previous studies. In Figure 10, we illustrate this by showing the best-fit line ($\log(N) = -3.52 + 0.34R$) to the the $20 < R < 24$ *R*-band galaxy counts presented in Gawiser et al. (2006). We also show the *r*-band galaxy number counts from SDSS (black curve limited to bright < 21 mag; Yasuda et al. 2001). We attribute the downturn in our number counts at $r > 24$ to incompleteness in our catalog. Our simulations indicate that our incompleteness is small for $r < 23.5$ and declines to 50% at $r = 24.5$. Consistent with our completeness simulations, our number counts

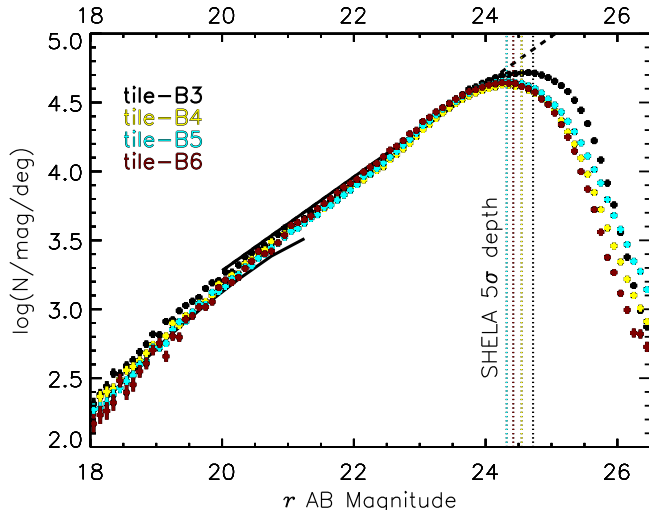


FIG. 10.— r -band differential galaxy number counts for each SHELA tile. For comparison we show the best-fit line ($\log(N) = -3.52 + 0.34R$) to the $20 < R < 24$ R -band galaxy counts presented in Gawiser et al. (2006). Their best-fit line is solid over the observed magnitude range and dashed for fainter magnitudes. We also show bright SDSS r -band galaxy counts ($r < 21.25$ black curve) from Yasuda et al. (2001). We attribute the downturn in our number counts at $r > 24$ to incompleteness in our catalog. We indicate our catalog’s 5σ depth with vertical dotted lines (see Section 3.6 for details)

indicate that our B3 tile is marginally deeper than our other tiles.

4. SPITZER/IRAC FORCED PHOTOMETRY FOR DECam-SELECTED SOURCES

In this section we describe how we construct a mixed-resolution multi-band catalog of DECam $ugriz$ + Spitzer/IRAC 3.6 and 4.5 μm bands. We generate an accurate multi-band catalog of DECam $ugriz$ + Spitzer/IRAC 3.6 and 4.5 μm bands by performing a “forced photometry with *The Tractor* image modeling code (Lang et al. 2016a,b). This technique employs prior measurements of source positions and surface brightness profiles from a high-resolution band to model and fit the fluxes of the source in the remaining bands. We specifically use *The Tractor* to optimize the likelihood for the photometric properties of DECam sources in both the IRAC 3.6 and 4.5 μm bands given initial information on the source obtained from DECam catalog and IRAC image parameters. Our approach allows us to detect extremely faint sources that fall well below the IRAC 5σ depth threshold of 22 AB mag (P16). Additionally, the improved DECam resolution allows us to accurately measure fluxes for blended IRAC sources.

4.1. Image Calibration Parameters and Input Catalog

We supply *The Tractor* with the input image of SHELA IRAC 3.6 and 4.5 μm images (P16) with corresponding image calibration information, including rms maps (noise model), the empirical IRAC point response function (PRFs), and image astrometric information (WCS). In addition, we supply our DECam catalog in each tile as an input catalog of prior source parameters, including source positions, brightness, and surface brightness profile shapes (effective radius, position angle, and axis ratio).

4.2. Surface Brightness Profile Modeling

Broadly speaking, *The Tractor* proceeds by rendering a model of a galaxy or a point source convolved with the IRAC PRF at each IRAC band and then performs a linear least-square fit for source fluxes such that the sum of source fluxes is closest to the actual image pixels, with respect to the noise model. Finally, the Tractor provides the measurement IRAC flux of each DECam source with the lowest reduced chi squared value (χ^2_{red}).

In practice, we extract IRAC 3.6 and 4.5 μm image cutouts of each DECam source. We select a cutout size of $20'' \times 20''$, which represents a trade-off between minimizing computational costs related to larger cutout sizes and ensuring that the contributing sources lie well within the cutout extent.

For each DECam source, we measure its IRAC fluxes with three brightness profiles: a point source profile, an exponential profile (equivalent to a Sérsic profile with $n = 1$), and a deVaucouleurs profile (equivalent to a Sérsic profile with $n = 4$). In our final output catalog, we report optimized IRAC fluxes and model profiles (0 = point source, 1 = exponential, and 4 = deVaucouleurs profile) that give the lowest reduced chi squared (χ^2_{red}) value. Objects with dubious Tractor photometry are assigned a non-zero Tractor flag. Specifically, Tractor flag values indicate 5σ outliers from the existing SHELA IRAC SExtractor catalog (flag = 1) and non-optimized Tractor extraction (flag = 2).

To avoid unphysical results due to optimizing too many sources parameters (i.e., source positions, shapes, and brightness) and the presence of crowded neighboring sources or bright and extended nearby sources, we perform *The Tractor* forced photometry twice for each DECam source of interest. We begin with identifying and masking out bright and extended DECam sources located within $20''$ from a source of interest. This includes masking out IRAC-only sources that are not detected in our DECam catalog. For the first optimization, we exclude the source of interest and other sources within $4''$ aperture radius from the modeling. The light profile of these neighboring sources located within a $4''$ aperture radius could potentially blend with that of a source of interest, and therefore we will simultaneously fit these neighboring sources and a source of interest during the second optimization. We simultaneously model all other neighboring sources located at distance $> 4''$ within the cutout by holding all image calibration parameters, positions, and surface brightness profile shapes of neighboring sources fixed except for their brightnesses, which is allowed to be optimized.

We then subtract the resulting modeled image cutout of neighboring sources from the IRAC image cutout, and are therefore left with the image of the source of interest and its neighboring sources located within $4''$ aperture radius.

For the second optimization, we run *The Tractor* on the IRAC “neighboring sources subtracted” cutout by holding all image calibration parameters fixed and allow source position, brightness, and effective radius (for an exponential profile or a deVaucouleurs profile) to be optimized. We allow the position of the source of interest to be varied within 1 arcsecond relative to the input source position from DECam catalog. In addition, if the mod-

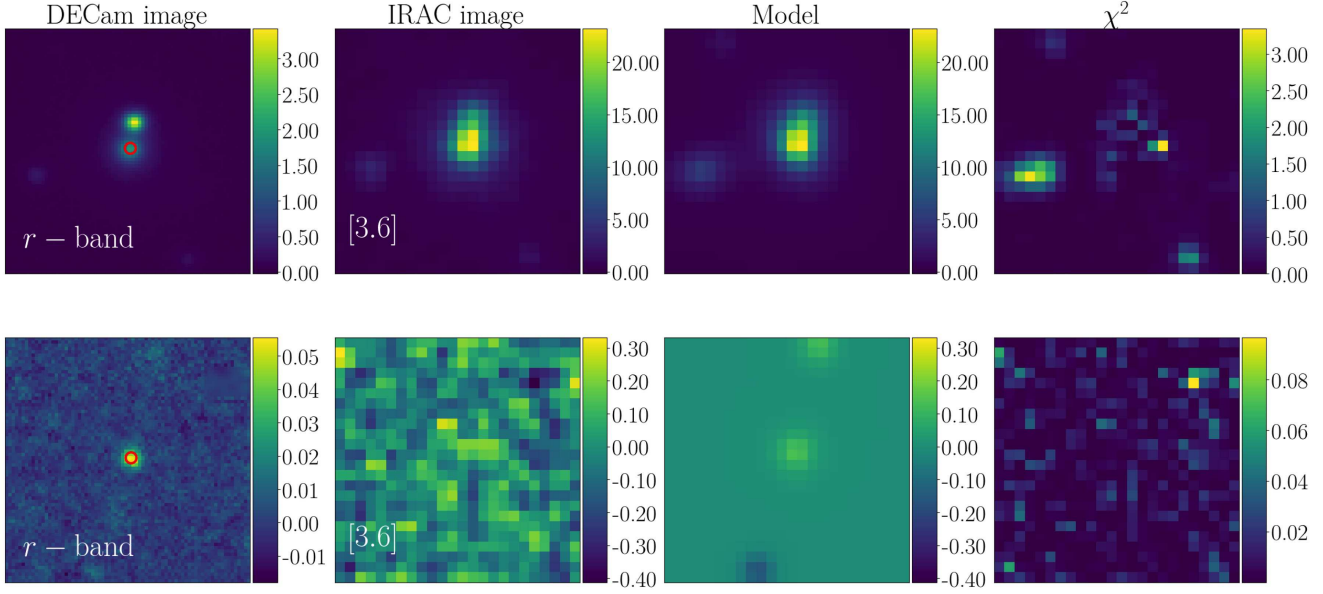


FIG. 11.— *Top*: Example of our forced photometry procedure for a source that is clearly blended in the IRAC $3.6\mu\text{m}$ image but resolved in the DECcam r -band image. The cutout dimensions are $20'' \times 20''$ and the source was modeled using a deVaucouleurs profile. The first two columns show the original images in DECcam r -band and IRAC $3.6\mu\text{m}$ band, respectively. The third column shows the source model convolved with the PRF of each IRAC band, and the fourth column shows the χ^2 residual maps. The colorbar units are μJy . We indicate the DECcam source whose IRAC photometry is measured as red circle symbol in the first column. *Bottom*: Example of a source with no blending issues, but that is undetected in the original IRAC-selected catalog (P16). The source was modeled using an exponential profile.

eled effective radius output from *The Tractor* is unphysical (i.e., a negative value), we then rerun *The Tractor* by fixing the effective radius to the input effective radius from DECcam catalog. Examples of the original multi-band images, models, and χ^2 maps for a blended IRAC source and a non-blended, faint IRAC source for which *The Tractor* has produced improved IRAC photometry are shown in Figure 11. We emphasize that the example of the faint source with a measurement based on our DECcam-selected forced photometry was not detected in the original SHELA IRAC SExtractor catalog. These examples demonstrate the ability of our forced photometry to detect extremely faint objects and sources known to be blended in the original SHELA IRAC catalog (P16).

4.3. Results

We find that about 47% of the sources in the DECcam-selected forced photometry catalogs are best modeled by spatially resolved surface brightness profiles (see Section 4.2). Of the resolved sources, the majority are best modeled by an exponential profile ($\sim 61\%$) rather than a deVaucouleurs profile ($\sim 39\%$).

To compare *The Tractor* forced photometry with the existing SHELA IRAC photometry, we make a catalog of DECcam-sources which are cross-matched with the P16 SHELA IRAC catalog within a search radius of $3''$ (995,607 objects in total). We identify blended sources in IRAC based on the presence of a nearby source in the DECcam catalog within $4''$ (about twice the angular resolution of the IRAC data), whereas sources lacking neighbors in DECcam within $4''$ are free of blending issues in IRAC. Based on these criteria, we expect at least 35% of the total sources in the DECcam input catalog will be blended in the 3.6 and $4.5\mu\text{m}$ IRAC mosaics. This

high fraction of blended sources in IRAC is one of the primary motivations for performing forced photometry with *The Tractor*.

In Figure 12, we show a comparison between the source magnitudes from *The Tractor* forced photometry and the original IRAC photometry measured in $6''$ -diameter apertures, corrected to total fluxes (P16). We find that our forced photometry is typically in good agreement with the SHELA IRAC magnitudes though some scatter is apparent, particularly for blended sources. The scatter is reduced when we restrict the comparison to “isolated” sources that lack a DECcam neighbor within $4''$. The median offsets between the *Tractor* and the IRAC aperture-corrected magnitudes are -0.12 , -0.06 , 0.45 for all, not blended, and blended sources brighter than 22 AB, respectively. We expect that the larger offset and scatter for blended sources are mainly due to the ability of our *The Tractor* force photometry procedure to de-blend those sources. The other contributing factors to the scatter could be spatial PSF variations, inaccurately matched sources in the DECcam and IRAC catalogs, and issues with the photometry from the original catalogs.

4.3.1. Error Estimates

The Tractor outputs errors on each optimized parameter, including source brightness. To ensure that *The Tractor* outputs a photometric error consistent with those from the existing SHELA IRAC photometric catalog (P16), we generate the rms map for *The Tractor* forced photometry procedure by taking the IRAC 3.6 and $4.5\mu\text{m}$ weight map and scaling C in a $C/\sqrt{(\text{weight map})}$ image such that the median photometric error output from *The Tractor* are roughly matched with those measured in $6''$ -diameter aperture, corrected to total. Here

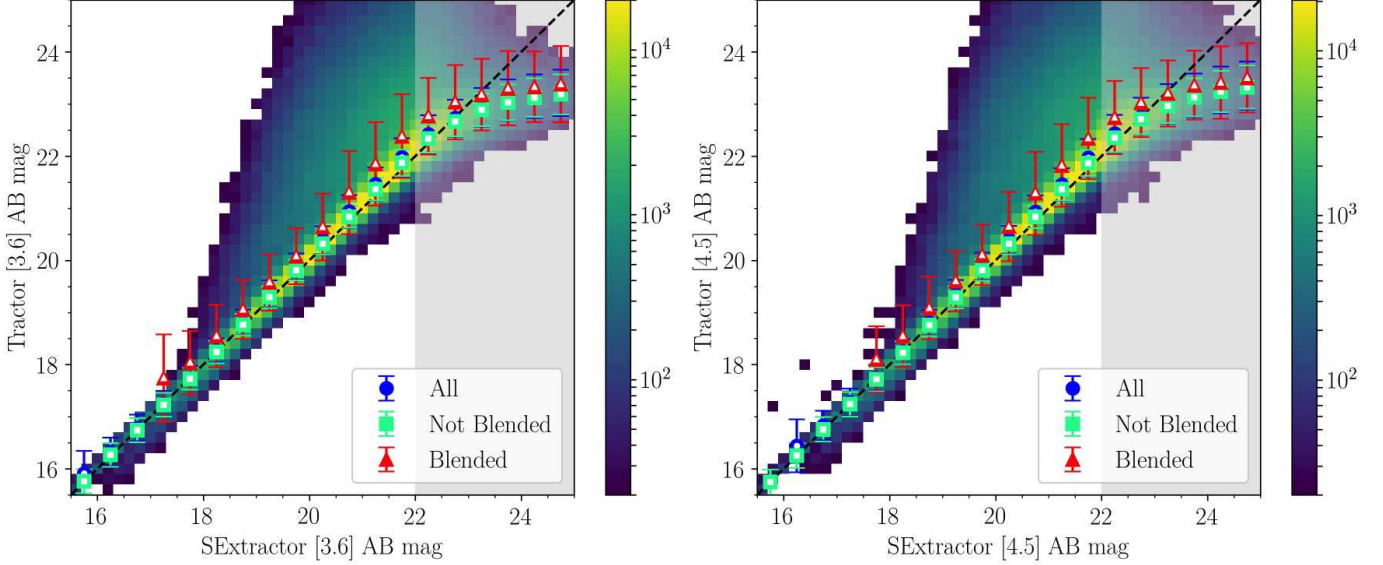


FIG. 12.— The comparison between *The Tractor* and original IRAC photometry measured in $6''$ -diameter apertures, corrected to total fluxes. The color scale represents the density of points for all sources matched between our DECam catalogs and the IRAC SExtractor catalog (P16). Data points with error bars show median Tractor IRAC magnitudes and corresponding standard deviation from median absolute deviations in bins of original IRAC magnitudes for all sources (blue circles), non-blended sources (green squares), and blended sources (red triangles). Blended IRAC sources are identified based on the presence of a nearby source in the DECam catalog within $4''$. Sources lacking neighbors in DECam within $4''$ are free of blending issues in IRAC. The dashed line shows the one-to-one correspondence between *The Tractor* and the P16 catalog magnitudes. The gray-shaded region highlights the parameter space below the 80% completeness limit (22.0 AB mag).

we adopt $C = 0.265$ and 0.287 as scaling factors for our in 3.6 or $4.5 \mu\text{m}$ rms images ($C/\sqrt{(\text{weight map})}$), respectively. Finally, we add the Tractor photometric error in quadrature with an additional error $\sigma_{\text{sys}} = 0.05$ mag to account for the median offset between the Tractor and the aperture-corrected magnitudes for non-blended sources. The total photometric error $\sigma_{i,c}$ on each DECam source i in IRAC channel c is then given by,

$$\sigma_{i,c}^2 = \sigma_{i,c,\text{forced phot}}^2 + (0.921\sigma_{\text{sys}} \times F_{i,c,\text{forced phot}})^2 \quad (13)$$

where $F_{i,c,\text{forced phot}}$ and $\sigma_{i,c,\text{forced phot}}$ are the flux density and its error measured from *The Tractor* forced photometry procedure.

4.4. Caveats

We emphasize that improved photometry of blended IRAC sources can only be achieved if the blended objects are well resolved in the DECam catalog. We also note that the accuracy of our photometry with *The Tractor* will be reduced for highly complex and extended sources that are not well described by an exponential galaxy profile or a deVaucouleurs model. Therefore, we provide a Tractor flag for each source to indicate failed extractions (flag= 2) and to indicate where the Tractor flux differs from the existing SHELA IRAC catalog by more than 5σ (flag= 1):

$$\frac{|f_{\text{Tractor}} - f_{\text{SExtractor}}|}{\sqrt{\sigma_{\text{Tractor}}^2 + \sigma_{\text{SExtractor}}^2}} > 5. \quad (14)$$

5. THE SHELA CATALOG

In Table 6, we show a sample of the final SHELA DECam catalog for tile B3. Our catalogs include DECam

PSF fluxes appropriate for unresolved sources and SExtractor MAG_AUTO fluxes for resolved sources along with ancillary morphology information as described in Section 3.4. As discussed in Section 3.7, we recommend excluding cataloged fluxes with internal SExtractor flag > 3 or cataloged fluxes with external SExtractor flag $> 0^{17}$. We also catalog J - and K -band MAG_AUTO fluxes from Geach et al. (2017) for sources with DECam counterparts within $r = 1''.5$. This archival near-infrared survey has 5σ point-source depths of $J = 21.4$ and $K = 20.9$. DECam sources without cataloged J - and K -band counterparts are assigned a NIR flux of ‘-99’. We list 3.6 and $4.5 \mu\text{m}$ IRAC Tractor fluxes and ancillary extraction parameters as discussed in Section 4. IRAC fluxes with Tractor flags > 1 indicate unreliable extractions. Finally, we list EAZY (Brammer et al. 2008) photometric redshift information which is discussed in the following section.

5.1. Photometric Redshifts

In Figure 13 we show our ability to measure photometric redshifts by comparing our dataset to the available $\langle z \rangle = 0.33$ SDSS spectroscopic redshifts. In the near future HETDEX will allow us to extend this analysis out to $z = 3.5$ by providing spectroscopic redshifts for a sample of $N \sim 200,000$ galaxies at $1.9 < z < 3.5$. For this work, we match all SDSS z_{spec} galaxies within $1''$ of our DECam/IRAC objects. We also utilize the archival J and K -band data from Geach et al. (2017). We use SExtractor FLUX_AUTO fluxes for the *ugrizJK*-bands and use

¹⁷ Given our catalog’s convention of rounding to the nearest thousandth decimal place for DECam fluxes, there are rare cases where the rounded DECam flux error equals “0.000”. All “0.000” flux error sources have non-zero flags indicating extraction problems and should be utilized with caution. To avoid null values, we adopt a minimum flux error of “0.001” for these sources.

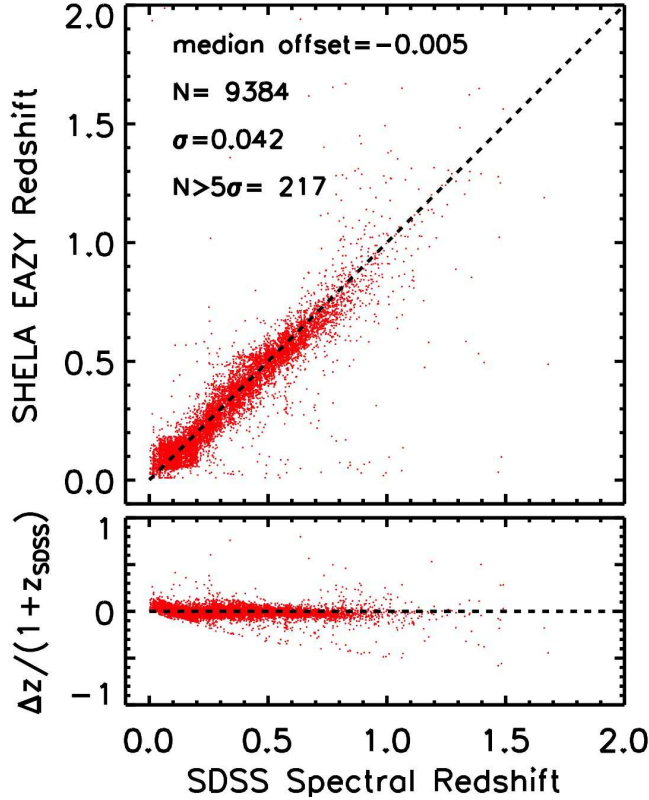


FIG. 13.— Our SHELA photometric z_{peak} redshifts versus SDSS spectroscopic redshifts.

Tractor fluxes for the IRAC bandpasses.

We use the photometric code EAZY (Brammer et al. 2008) to estimate redshifts from our merged SHELA catalog. We require measured objects to have 5 valid flux measurements, and we utilized EAZY’s option to apply a K -band magnitude prior. As discussed in Section 3.7, we find that the purity of our DECam catalog is improved by excluding fluxes with internal SExtractor flags > 3 and external SExtractor flags > 0 . Additionally, we exclude all IRAC fluxes with Tractor flags > 1 which indicate extraction errors. For the purposes of running EAZY, we assign these flagged fluxes a large negative number that is below EAZY’s NOT_OBS_THRESHOLD.

We display EAZY’s z_{peak} parameter in Figure 13. This parameter corresponds to the peak probability of the $P(z)$ function, and is considered the most accurate z_{photo} estimate (Muzzin et al. 2013). We find that the median $\Delta z = z_{\text{photo}} - z_{\text{spec}}$ is -0.005 and the normalized median absolute deviation, defined as:

$$\sigma_{\text{NMAD}} = 1.48 \times \text{median} \left(\left| \frac{\Delta z - \text{median}(\Delta z)}{1 + z_{\text{spec}}} \right| \right), \quad (15)$$

is 0.042 with 2.3% of sources found to be 5σ outliers. We find that our photometric results are comparable to those reported in the EAZY test fields (Brammer et al. 2008). Here K -selected $UBVIJHK$ +IRAC catalogs in CDF-South and other deep fields were found to have median $\Delta z = -0.005$ and $\sigma_{\text{NMAD}} = 0.034$ with 5% of the sources found to be 5σ outliers for $0 < z < 6$ galaxies. Future work will improve on our preliminary z_{photo} estimates by incorporating HETDEX spectroscopic red-

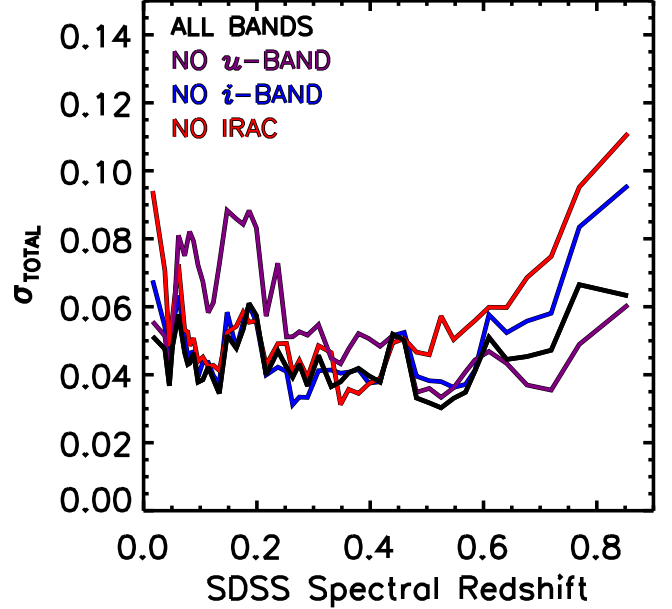


FIG. 14.— Total photometric z_{peak} redshift error versus SDSS spectroscopic redshift.

shifts from $\sim 200,000$ Ly α emitters at $1.9 < z < 3.5$ and $\sim 200,000$ [OII] emitters at $z < 0.5$.

In addition to z_{peak} , we also catalog the EAZY redshift where χ^2 is minimized for the all-template linear combination model without applying a prior (z_a) and the corresponding minimum χ^2 value (χ_a^2). Removing the prior lessens the importance of the K -band data and may produce favorable results for K -band faint objects ($K \gtrsim 20.9$).

Our catalog adds to existing surveys like DECaLS by providing deep u -band and i -band measurements along with IRAC measurements for all detected DECam sources in the SHELA field. In Figure 14, we show how the total photometric redshift error (σ_{TOTAL}) is altered if we re-run EAZY with a DECam bandpass or both IRAC bandpasses excluded from our catalog. For each EAZY run we keep all input parameters the same with the exception of the required number of observed bandpasses (N_MIN_COLORS) which we reduce by the number of excluded bandpasses to ensure that we are able to compare the same sample of $N = 9384$ galaxies in each run. We estimate the total photometric redshift error by adding in quadrature the random error as measured by σ_{NMAD} with the systematic error as measured by $\text{median}(\Delta z)$. We require each redshift bin to have $N = 200$ galaxies, which restricts our analysis to $z < 1$. Excluding the u -band worsens total-sigma for $z < 0.4$ by increasing the σ_{NMAD} term. Excluding IRAC or to a lesser extent the i -band worsens total-sigma for $z > 0.4$ by increasing the $\text{median}(\Delta z)$ term. Only by including all available bandpasses are we able to maintain $\sigma_{\text{TOTAL}} \sim 0.05$ for our $z < 1$ SDSS sample.

6. SUMMARY

SHELA’s deep, wide-area multi-wavelength images – spanning a wavelength range of 0.35 to $4.5 \mu\text{m}$ – combined with HETDEX’s spectroscopic information will enable many extragalactic studies, including measuring the evolution of galaxy stellar mass, halo mass, and environ-

ment from $1.5 < z < 3.5$. In this paper, we presented *ugirz*-band DECam catalogs that reach a 5σ depth of ~ 24.5 AB mag and cover 17.5 deg^2 of the overall SHELA field. We performed IRAC forced photometry with *The Tractor* image modeling code to measure 3.6 and $4.5 \mu\text{m}$ fluxes for all objects within our DECam catalog. For our DECam sub-catalog, we demonstrated consistency with the DECaLS DR5 and the DES DR1. We showed that our computed galaxy number counts and photometric redshift errors are consistent with previous studies.

Ultimately, we plan to tile all of the available DES *griz*-band data over the full HETDEX fall field, which has a 224 deg^2 FOV centered at $\alpha, \delta = 22.5 \text{ deg}, 0 \text{ deg}$. The completed DECam survey for the HETDEX fall field will have tiles ranging from A1 to C10 and will encompass the presented tiles, B3-B6.

We thank the anonymous referee for comments that substantially improved the manuscript. The authors wish to thank Dustin Lang, John Moustakas, Niv Drory, Karl Gebhardt, and Rachael Livermore for insightful discussions. IGBW and SLF acknowledge support from the National Science Foundation through grants AST 1518183 and 1614798. LK and CP acknowledge support from the National Science Foundation through grants AST 1413317 and 1614668. LK thanks the LSSTC Data Science Fellowship Program, her time as a Fellow has benefited this work. This research draws upon data provided by the NOAO Science Archive. NOAO is operated by the Association of Universities for Research in Astronomy (AURA), Inc. under a cooperative agreement with the National Science Foundation. This work is based in part on observations made with the *Spitzer Space Telescope*, which is operated by the Jet Propulsion Laboratory, California Institute of Technology under a contract with NASA. The authors acknowledge the Texas Advanced Computing Center (TACC) at The University of Texas at Austin for providing HPC resources that have contributed to the research results reported within this paper. URL: <http://www.tacc.utexas.edu>.

This project used data obtained with the Dark Energy Camera (DECam), which was constructed by the Dark Energy Survey (DES) collaboration. Funding for the DES Projects has been provided by the U.S. Department of Energy, the U.S. National Science Foundation, the Ministry of Science and Education of Spain, the Science and Technology Facilities Council of the United Kingdom, the Higher Education Funding Council for England, the National Center for Supercomputing Applications at the University of Illinois at Urbana-Champaign, the Kavli Institute of Cosmological Physics at the University of Chicago, the Center for Cosmology and Astro-Particle Physics at the Ohio State University, the Mitchell Institute for Fundamental Physics and Astronomy at Texas A&M University, Financiadora de Estudos e Projetos, Fundação Carlos Chagas Filho de Amparo à Pesquisa do Estado do Rio de Janeiro, Conselho Nacional de Desenvolvimento Científico e Tecnológico and the Ministério da Ciência, Tecnologia e Inovação, the Deutsche Forschungsgemeinschaft, and the Collaborating Institutions in the Dark Energy Survey. The Collaborating Institutions are Argonne National Laboratory, the University of California at Santa Cruz,

the University of Cambridge, Centro de Investigaciones Energéticas, Medioambientales y Tecnológicas-Madrid, the University of Chicago, University College London, the DES-Brazil Consortium, the University of Edinburgh, the Eidgenössische Technische Hochschule (ETH) Zürich, Fermi National Accelerator Laboratory, the University of Illinois at Urbana-Champaign, the Institut de Ciències de l'Espai (IEEC/CSIC), the Institut de Física d'Altes Energies, Lawrence Berkeley National Laboratory, the Ludwig-Maximilians Universität München and the associated Excellence Cluster Universe, the University of Michigan, the National Optical Astronomy Observatory, the University of Nottingham, the Ohio State University, the OzDES Membership Consortium the University of Pennsylvania, the University of Portsmouth, SLAC National Accelerator Laboratory, Stanford University, the University of Sussex, and Texas A&M University.

Based on observations at Cerro Tololo Inter-American Observatory, National Optical Astronomy Observatory (NOAO Prop. ID 2013B-0438; and PI: C. Papovich), which is operated by the Association of Universities for Research in Astronomy (AURA) under a cooperative agreement with the National Science Foundation.

This project used data from the DECam Legacy Survey. The Legacy Surveys consist of three individual and complementary projects: the Dark Energy Camera Legacy Survey (DECaLS; NOAO Proposal ID 2014B-0404; PIs: David Schlegel and Arjun Dey), the Beijing-Arizona Sky Survey (BASS; NOAO Proposal ID 2015A-0801; PIs: Zhou Xu and Xiaohui Fan), and the Mayall z-band Legacy Survey (MzLS; NOAO Proposal ID 2016A-0453; PI: Arjun Dey). DECaLS, BASS and MzLS together include data obtained, respectively, at the Blanco telescope, Cerro Tololo Inter-American Observatory, National Optical Astronomy Observatory (NOAO); the Bok telescope, Steward Observatory, University of Arizona; and the Mayall telescope, Kitt Peak National Observatory, NOAO. The Legacy Surveys project is honored to be permitted to conduct astronomical research on Iolkam Du'ag (Kitt Peak), a mountain with particular significance to the Tohono O'odham Nation.

This work made use of data from SDSS. Funding for the Sloan Digital Sky Survey IV has been provided by the Alfred P. Sloan Foundation, the U.S. Department of Energy Office of Science, and the Participating Institutions. SDSS-IV acknowledges support and resources from the Center for High-Performance Computing at the University of Utah. The SDSS web site is www.sdss.org.

SDSS-IV is managed by the Astrophysical Research Consortium for the Participating Institutions of the SDSS Collaboration including the Brazilian Participation Group, the Carnegie Institution for Science, Carnegie Mellon University, the Chilean Participation Group, the French Participation Group, Harvard-Smithsonian Center for Astrophysics, Instituto de Astrofísica de Canarias, The Johns Hopkins University, Kavli Institute for the Physics and Mathematics of the Universe (IPMU) / University of Tokyo, the Korean Participation Group, Lawrence Berkeley National Laboratory, Leibniz Institut für Astrophysik Potsdam (AIP), Max-Planck-Institut für Astronomie (MPIA Heidelberg), Max-Planck-Institut für Astrophysik (MPA Garching), Max-Planck-Institut für Extraterrestrische

Physik (MPE), National Astronomical Observatories of China, New Mexico State University, New York University, University of Notre Dame, Observatório Nacional / MCTI, The Ohio State University, Pennsylvania State University, Shanghai Astronomical Observatory, United Kingdom Participation Group, Universidad

Nacional Autónoma de México, University of Arizona, University of Colorado Boulder, University of Oxford, University of Portsmouth, University of Utah, University of Virginia, University of Washington, University of Wisconsin, Vanderbilt University, and Yale University.

REFERENCES

- Abbott, T. M. C., Abdalla, F. B., Allam, S., et al. 2018, *ApJS*, 239, 18
- Bertin, E., & Arnouts, S. 1996, *A&AS*, 117, 393
- Bertin, E., Mellier, Y., Radovich, M., et al. 2002, in *Astronomical Society of the Pacific Conference Series*, Vol. 281, *Astronomical Data Analysis Software and Systems XI*, ed. D. A. Bohlender, D. Durand, & T. H. Handley, 228
- Brammer, G. B., van Dokkum, P. G., & Coppi, P. 2008, *ApJ*, 686, 1503
- Brunner, R. J., Connolly, A. J., Szalay, A. S., & Bershad, M. A. 1997, *ApJ*, 482, L21
- Dark Energy Survey Collaboration, Abbott, T., Abdalla, F. B., et al. 2016, *MNRAS*, 460, 1270
- Flaugher, B., Diehl, H. T., Honscheid, K., et al. 2015, *AJ*, 150, 150
- Gawiser, E., van Dokkum, P. G., Herrera, D., et al. 2006, *ApJS*, 162, 1
- Geach, J. E., Lin, Y.-T., Makler, M., et al. 2017, *ApJS*, 231, 7
- Hill, G. J., Gebhardt, K., Komatsu, E., et al. 2008, in *Astronomical Society of the Pacific Conference Series*, Vol. 399, *Panoramic Views of Galaxy Formation and Evolution*, ed. T. Kodama, T. Yamada, & K. Aoki, 115
- Honscheid, K., DePoy, D. L., & for the DES Collaboration. 2008, *ArXiv e-prints*
- Keenan, R. C., Trouille, L., Barger, A. J., Cowie, L. L., & Wang, W.-H. 2010, *ApJS*, 186, 94
- Kurucz, R. L. 1993, *SYNTH* spectrum synthesis programs and line data
- Lang, D., Hogg, D. W., & Mykytyn, D. 2016a, *The Tractor: Probabilistic astronomical source detection and measurement*, *Astrophysics Source Code Library*
- Lang, D., Hogg, D. W., & Schlegel, D. J. 2016b, *AJ*, 151, 36
- Lupton, R., Gunn, J. E., Ivezić, Z., Knapp, G. R., & Kent, S. 2001, in *Astronomical Society of the Pacific Conference Series*, Vol. 238, *Astronomical Data Analysis Software and Systems X*, ed. F. R. Harnden, Jr., F. A. Primini, & H. E. Payne, 269
- Muzzin, A., Marchesini, D., Stefanon, M., et al. 2013, *ApJS*, 206, 8
- Ouchi, M., Shimasaku, K., Okamura, S., et al. 2004, *ApJ*, 611, 660
- Papovich, C., Shipley, H. V., Mehrrens, N., et al. 2016, *ApJS*, 224, 28
- Yasuda, N., Fukugita, M., Narayanan, V. K., et al. 2001, *AJ*, 122, 1104
- Zacharias, N., Finch, C. T., Girard, T. M., et al. 2013, *AJ*, 145, 44

TABLE 6
SHELA DECAM CATALOG SAMPLE

ID	R.A.(J2000)	decl.(J2000)	a	e	θ	r_{Kron}	$r_{1/2}$	f_u^{PSF}	σ_u^{PSF}	f_u^{AUTO}	σ_u^{AUTO}	Internal	External
(1)	(deg)	(deg)	(arcsec)	(5)	(deg)	(7)	(8)	(μJy)	(μJy)	(μJy)	(μJy)	u Flag	u Flag
(1)	(2)	(3)	(4)	(5)	(6)	(7)	(8)	(9)	(10)	(11)	(12)	(13)	(14)
B3_342206	15.527544	0.953232	0.4	0.11	-78.5	4.5	0.8	0.126	0.079	0.139	0.130	0	0
B3_342207	15.527545	-0.920483	2.2	0.17	-6.2	3.5	1.6	3.467	0.166	8.813	0.598	2	0
B3_342208	15.527546	0.045727	1.0	0.43	29.3	5.3	1.4	0.374	0.050	0.767	0.213	3	0
B3_342209	15.527547	-0.864834	0.5	0.09	-40.9	6.7	1.7	0.084	0.055	0.069	0.174	3	0
B3_342210	15.527553	-0.486625	0.3	0.21	-88.8	8.2	0.8	0.285	0.048	0.319	0.077	0	0
B3_342211	15.527553	0.914503	0.6	0.14	29.3	3.5	0.8	0.421	0.070	0.428	0.105	0	0
B3_342212	15.527556	-0.541192	0.8	0.13	14.3	4.3	1.1	0.659	0.059	1.045	0.180	0	0
B3_342213	15.527563	-0.312693	0.4	0.23	58.4	5.5	0.7	0.057	0.046	0.067	0.079	0	0
B3_342214	15.527564	-0.485899	0.6	0.14	20.9	6.0	1.1	0.431	0.048	0.660	0.160	0	0
B3_342215	15.527565	0.217230	0.3	0.29	-75.0	8.7	1.2	0.064	0.047	0.040	0.089	0	0
B3_342216	15.527566	0.452349	0.8	0.01	-85.6	3.5	0.7	1.462	0.087	1.364	0.152	0	0
B3_342217	15.527570	0.760209	0.4	0.11	16.8	6.9	1.2	0.039	0.054	-0.042	0.156	0	0
B3_342218	15.527570	0.148665	0.3	0.53	8.6	9.1	0.9	0.141	0.045	0.077	0.062	0	0
B3_342219	15.527574	-0.484608	0.5	0.22	-33.5	5.3	0.9	0.455	0.049	0.476	0.090	0	0
B3_342220	15.527574	0.871303	0.7	0.09	31.0	4.1	0.9	0.187	0.048	0.062	0.119	0	0
B3_342221	15.527574	0.801912	0.6	0.13	-35.7	4.5	0.9	0.172	0.045	0.325	0.118	0	0
B3_342222	15.527575	-0.923096	0.4	0.59	45.0	9.3	1.4	0.050	0.050	0.158	0.097	1	0
B3_342223	15.527581	-0.587486	0.7	0.19	-32.8	6.7	2.2	0.224	0.051	0.240	0.253	3	0
B3_342224	15.527582	-0.459715	0.3	0.22	-16.2	7.3	0.9	0.130	0.050	0.169	0.099	0	0
B3_342225	15.527587	0.983389	1.1	0.13	35.9	3.7	1.3	1.121	0.112	2.540	0.405	0	0
B3_342226	15.527598	0.186228	0.7	0.15	-66.3	3.5	0.8	0.584	0.054	0.716	0.099	0	0
B3_342227	15.527602	0.923314	0.4	0.12	-84.7	7.5	1.3	0.468	0.063	0.590	0.186	0	0
B3_342228	15.527604	0.230341	0.6	0.11	6.1	3.9	0.8	0.726	0.058	0.651	0.106	0	0
B3_342229	15.527604	-0.855998	0.3	0.26	20.9	8.2	0.7	0.061	0.051	-0.005	0.077	0	0
B3_342230	15.527604	-0.146012	0.3	0.27	-20.3	7.9	0.7	0.075	0.046	-0.023	0.067	0	0
B3_342231	15.527611	0.581601	0.5	0.20	58.6	5.2	0.8	0.470	0.062	0.252	0.114	0	0
B3_342232	15.527616	-0.157985	0.5	0.16	44.0	5.8	0.9	0.240	0.048	0.326	0.121	0	0
B3_342233	15.527617	0.386069	0.4	0.01	-31.2	4.4	0.8	0.312	0.049	0.318	0.080	0	0
B3_342234	15.527618	-0.708591	0.6	0.35	-58.7	3.5	0.8	0.418	0.054	0.369	0.073	0	0
B3_342235	15.527623	-0.015360	0.4	0.20	-19.0	6.5	0.9	0.140	0.045	0.238	0.096	0	0
B3_342236	15.527623	-0.849101	1.0	0.23	-19.9	4.1	1.2	0.661	0.055	1.690	0.204	0	0
B3_342237	15.527628	0.790137	1.0	0.04	25.0	3.5	1.1	2.394	0.120	3.911	0.246	0	0
B3_342238	15.527630	0.211697	0.7	0.00	83.7	5.3	1.2	-0.005	0.044	-0.120	0.165	3	0
B3_342239	15.527635	0.867821	0.4	0.18	-64.1	6.7	0.9	0.123	0.060	0.050	0.126	0	0
B3_342240	15.527637	0.109887	0.1	0.09	-45.1	8.9	0.7	0.155	0.045	0.121	0.042	2	0
B3_342241	15.527639	0.490189	0.7	0.13	73.3	5.8	1.1	0.621	0.053	0.810	0.178	3	0
B3_342242	15.527645	0.741641	0.5	0.22	4.7	7.4	1.5	0.151	0.055	0.265	0.180	1	0
B3_342243	15.527646	-1.025758	1.3	0.34	43.4	3.5	1.2	5.255	0.251	9.989	0.534	3	0
B3_342244	15.527649	-0.386170	0.5	0.25	60.4	4.3	0.8	0.233	0.048	0.325	0.080	3	0
B3_342245	15.527656	-0.129023	1.3	0.43	-12.4	3.6	1.1	0.253	0.048	0.550	0.171	0	0
B3_342246	15.527657	-0.054396	0.2	0.41	-18.4	9.1	0.7	0.075	0.044	0.097	0.050	0	0
B3_342247	15.527658	0.506951	0.8	0.13	25.5	3.8	0.9	1.881	0.100	2.138	0.169	0	0
B3_342248	15.527661	-0.046701	1.0	0.18	34.4	3.5	0.9	8.493	0.396	9.649	0.481	0	0
B3_342249	15.527661	-0.508430	0.8	0.26	69.4	3.5	0.9	0.512	0.050	0.627	0.100	0	0
B3_342250	15.527662	0.479859	0.5	0.18	-27.8	7.0	1.1	0.071	0.047	0.066	0.137	0	0
B3_342251	15.527669	-0.250235	0.2	0.38	0.4	9.0	0.6	0.082	0.047	0.074	0.047	0	0

TABLE 6
SHELA DECam CATALOG SAMPLE (CONTINUED)

f_g^{PSF} (μJy) (15)	σ_g^{PSF} (μJy) (16)	f_g^{AUTO} (μJy) (17)	σ_g^{AUTO} (μJy) (18)	Internal g Flag (19)	External g Flag (20)	f_r^{PSF} (μJy) (21)	σ_r^{PSF} (μJy) (22)	f_r^{AUTO} (μJy) (23)	σ_r^{AUTO} (μJy) (24)	Internal r Flag (25)	External r Flag (26)
0.144	0.077	0.017	0.122	0	0	0.515	0.107	0.491	0.181	0	0
15.871	0.734	38.123	1.858	2	0	56.910	2.622	130.260	6.062	2	0
0.399	0.063	0.489	0.256	3	0	0.490	0.080	1.018	0.382	3	0
0.264	0.069	0.430	0.206	3	0	0.559	0.088	0.896	0.292	3	0
0.300	0.070	0.245	0.109	0	0	0.380	0.091	0.430	0.153	0	0
0.424	0.068	0.461	0.100	0	0	0.689	0.095	0.687	0.148	0	0
0.763	0.071	1.130	0.206	0	0	1.352	0.106	2.195	0.333	0	0
0.186	0.066	0.190	0.108	0	0	0.454	0.096	0.370	0.168	0	0
0.724	0.071	1.177	0.217	0	0	1.104	0.103	1.692	0.353	0	0
0.087	0.059	0.212	0.107	0	0	0.322	0.079	0.475	0.155	0	0
13.339	0.618	12.903	0.616	0	0	49.914	2.300	47.510	2.200	0	0
0.149	0.059	0.133	0.160	0	0	0.311	0.091	0.849	0.282	0	0
0.225	0.058	0.129	0.079	0	0	0.280	0.090	0.368	0.131	0	0
0.490	0.066	0.587	0.123	0	0	0.683	0.095	0.732	0.189	0	0
0.114	0.061	-0.052	0.147	0	0	0.745	0.085	0.891	0.213	0	0
0.253	0.060	0.441	0.151	0	0	0.640	0.083	0.621	0.220	0	0
0.113	0.071	0.263	0.133	1	0	0.299	0.083	0.751	0.170	1	0
0.197	0.066	0.517	0.315	3	0	0.761	0.089	2.352	0.472	3	0
0.217	0.063	0.224	0.121	0	0	0.355	0.079	0.352	0.163	0	0
1.835	0.117	3.818	0.348	0	0	3.813	0.211	8.024	0.623	0	0
0.615	0.067	0.623	0.122	0	0	1.369	0.106	1.485	0.194	0	0
0.455	0.068	0.757	0.194	0	0	0.537	0.093	1.130	0.304	0	0
0.847	0.069	0.941	0.125	0	0	1.264	0.100	1.328	0.197	0	0
0.001	0.068	-0.036	0.100	0	0	0.306	0.078	0.259	0.121	0	0
0.065	0.065	0.032	0.091	0	0	0.349	0.095	0.345	0.141	0	0
0.441	0.065	0.395	0.117	0	0	0.538	0.104	0.616	0.209	0	0
0.276	0.064	0.300	0.153	0	0	0.547	0.093	0.655	0.245	0	0
0.373	0.061	0.367	0.097	0	0	0.432	0.080	0.482	0.138	0	0
0.626	0.068	0.615	0.089	0	0	0.706	0.092	0.797	0.129	0	0
0.242	0.055	0.345	0.113	0	0	0.382	0.079	0.399	0.176	0	0
0.960	0.077	1.859	0.255	0	0	1.919	0.117	3.195	0.369	0	0
4.083	0.198	6.438	0.364	0	0	7.759	0.367	12.786	0.671	0	0
0.122	0.059	0.792	0.209	3	0	0.634	0.083	1.554	0.321	3	0
0.067	0.060	0.076	0.123	0	0	0.292	0.078	0.281	0.173	0	0
0.236	0.058	0.219	0.054	2	0	0.371	0.099	0.320	0.094	2	0
0.744	0.075	1.226	0.254	3	0	1.022	0.090	1.691	0.339	3	0
0.237	0.069	0.560	0.215	1	0	0.424	0.084	0.986	0.296	1	0
11.033	0.516	20.573	1.012	3	0	18.888	0.878	33.499	1.637	3	0
0.323	0.064	0.400	0.104	3	0	0.675	0.089	0.644	0.149	3	0
1.523	0.091	2.490	0.226	0	0	5.391	0.260	8.575	0.497	0	0
0.102	0.056	0.103	0.061	0	0	0.332	0.093	0.289	0.106	0	0
2.035	0.109	2.228	0.179	0	0	2.510	0.155	2.926	0.329	0	0
15.220	0.704	18.248	0.860	0	0	27.002	1.246	31.261	1.468	0	0
0.755	0.067	0.848	0.126	0	0	1.640	0.108	1.904	0.198	0	0
0.161	0.060	0.209	0.167	0	0	0.508	0.081	0.718	0.244	0	0
0.113	0.062	0.084	0.062	0	0	0.358	0.083	0.297	0.085	0	0

TABLE 6
SHELA DECam CATALOG SAMPLE (CONTINUED)

f_i^{PSF} (μJy) (27)	σ_i^{PSF} (μJy) (28)	f_i^{AUTO} (μJy) (29)	σ_i^{AUTO} (μJy) (30)	Internal i Flag (31)	External i Flag (32)	f_z^{PSF} (μJy) (33)	σ_z^{PSF} (μJy) (34)	f_z^{AUTO} (μJy) (35)	σ_z^{AUTO} (μJy) (36)	Internal z Flag (37)	External z Flag (38)	VICS82ID Geach+17 (39)	f_j^{AUTO} (μJy) (40)	σ_j^{AUTO} (μJy) (41)
0.823	0.149	0.654	0.258	0	0	1.818	0.212	2.272	0.369	0	0	VICS82J010206.62+005712.0	-99.00	-99.00
91.047	4.195	203.426	9.471	2	0	119.496	5.506	265.109	12.401	2	0	VICS82J010206.61-005513.7	367.53	1.58
1.175	0.130	2.516	0.628	3	0	1.847	0.197	2.917	0.987	3	0	VICS82J010206.54+000245.7	3.13	0.57
1.106	0.130	1.617	0.436	3	0	1.285	0.210	1.576	0.760	3	0	...	-99.00	-99.00
0.345	0.147	0.288	0.256	0	0	0.565	0.203	0.598	0.364	0	0	...	-99.00	-99.00
1.349	0.140	1.423	0.216	0	0	2.110	0.195	2.094	0.301	0	0	VICS82J010206.59+005452.4	8.86	4.04
2.957	0.181	3.891	0.500	0	0	3.829	0.267	5.345	0.859	0	0	...	-99.00	-99.00
0.532	0.132	0.641	0.241	0	0	0.863	0.243	0.806	0.453	0	0	...	-99.00	-99.00
1.060	0.154	1.679	0.601	0	0	1.439	0.212	1.685	0.866	0	0	...	-99.00	-99.00
0.413	0.119	0.941	0.247	0	0	0.366	0.178	0.633	0.377	0	0	VICS82J010206.70+001302.0	-99.00	-99.00
148.397	6.835	143.257	6.606	0	0	226.570	10.436	218.371	10.075	0	0	VICS82J010206.60+002708.8	301.48	1.83
0.978	0.146	0.992	0.455	0	0	2.090	0.195	2.042	0.582	0	0	VICS82J010206.61+004536.5	-99.00	-99.00
0.540	0.133	0.546	0.197	0	0	0.413	0.182	0.305	0.278	0	0	...	-99.00	-99.00
0.398	0.147	0.570	0.317	0	0	0.339	0.174	0.097	0.387	0	0	...	-99.00	-99.00
2.616	0.166	3.230	0.355	0	0	4.423	0.265	5.056	0.549	0	0	VICS82J010206.62+005216.7	8.89	1.55
1.635	0.138	1.923	0.355	0	0	3.595	0.239	5.010	0.578	0	0	VICS82J010206.63+004806.9	-99.00	-99.00
0.382	0.120	0.981	0.255	1	0	0.819	0.177	1.770	0.384	1	0	...	-99.00	-99.00
0.877	0.126	3.092	0.733	3	0	0.954	0.226	3.431	1.425	3	0	...	-99.00	-99.00
0.448	0.121	0.606	0.262	0	0	0.767	0.242	0.561	0.540	0	0	...	-99.00	-99.00
4.531	0.313	8.712	1.129	0	0	5.813	0.359	10.852	1.241	0	0	VICS82J010206.63+005900.5	-99.00	-99.00
2.483	0.168	2.828	0.300	0	0	3.063	0.271	3.295	0.545	0	0	VICS82J010206.62+001110.5	3.74	0.69
0.461	0.140	0.864	0.488	0	0	0.574	0.171	0.218	0.617	0	0	...	-99.00	-99.00
2.097	0.152	2.179	0.298	0	0	2.839	0.220	3.164	0.460	0	0	VICS82J010206.59+001349.4	1.59	0.41
0.428	0.121	0.455	0.194	0	0	0.161	0.201	-0.014	0.333	0	0	...	-99.00	-99.00
0.458	0.128	0.277	0.195	0	0	0.410	0.232	0.530	0.363	0	0	...	-99.00	-99.00
0.732	0.135	0.676	0.278	0	0	0.862	0.182	0.439	0.386	0	0	...	-99.00	-99.00
0.937	0.135	1.262	0.370	0	0	1.657	0.211	1.833	0.586	0	0	...	-99.00	-99.00
0.846	0.124	0.891	0.218	0	0	0.943	0.182	1.121	0.334	0	0	...	-99.00	-99.00
0.666	0.123	0.634	0.179	0	0	0.629	0.176	0.659	0.264	0	0	...	-99.00	-99.00
0.491	0.140	0.758	0.329	0	0	0.936	0.178	0.790	0.424	0	0	...	-99.00	-99.00
4.270	0.230	7.930	0.671	0	0	6.871	0.361	11.901	1.019	0	0	VICS82J010206.64-005056.5	20.60	0.98
9.555	0.455	16.167	0.884	0	0	10.931	0.542	18.510	1.209	0	0	VICS82J010206.61+004724.1	10.67	1.26
3.051	0.183	4.207	0.543	3	0	6.861	0.362	7.645	0.874	3	0	VICS82J010206.63+001242.2	11.71	0.71
0.587	0.117	0.785	0.267	0	0	0.729	0.172	0.895	0.408	0	0	...	-99.00	-99.00
0.267	0.130	0.242	0.125	2	0	0.292	0.178	0.178	0.173	2	0	...	-99.00	-99.00
2.081	0.169	2.989	0.648	3	0	2.669	0.242	3.636	1.008	3	0	...	-99.00	-99.00
0.707	0.135	1.280	0.498	1	0	0.471	0.179	0.943	0.702	1	0	...	-99.00	-99.00
26.141	1.217	45.376	2.255	3	0	28.413	1.436	50.483	3.757	3	0	VICS82J010206.64-010132.5	59.93	1.76
0.940	0.138	1.034	0.242	3	0	1.219	0.182	1.314	0.327	3	0	...	-99.00	-99.00
11.234	0.530	18.388	0.974	0	0	14.912	0.714	24.075	1.395	0	0	VICS82J010206.64-000745.2	16.91	0.45
0.341	0.128	0.276	0.149	0	0	0.452	0.171	0.412	0.201	0	0	...	-99.00	-99.00
3.768	0.217	4.609	0.451	0	0	4.707	0.280	6.327	0.634	0	0	VICS82J010206.62+003025.5	6.15	0.84
38.803	1.791	44.759	2.102	0	0	40.377	1.870	46.205	2.248	0	0	VICS82J010206.63-000247.9	57.53	0.57
3.213	0.196	3.654	0.352	0	0	3.514	0.237	3.656	0.461	0	0	VICS82J010206.59-003030.2	3.27	0.44
0.516	0.133	0.876	0.431	0	0	0.443	0.182	0.948	0.622	0	0	...	-99.00	-99.00
0.141	0.119	0.100	0.124	0	0	-0.001	0.173	-0.051	0.182	0	0	VICS82J010206.68-001502.0	-99.00	-99.00

TABLE 6
SHELA DECam CATALOG SAMPLE (CONTINUED)

f_K^{AUTO} (μJy) (42)	σ_K^{AUTO} (μJy) (43)	$f_{3.6}$ (μJy) (44)	$\sigma_{3.6}$ (μJy) (45)	model _{3.6} (46)	log($P_{3.6}$) (47)	Tractor 3.6 Flag (48)	$f_{4.5}$ (μJy) (49)	$\sigma_{4.5}$ (μJy) (50)	model _{4.5} (51)	log($P_{4.5}$) (52)	Tractor 4.5 Flag (53)	z_{spec} SDSS (54)	z_{peak} EAZY (55)	z_a EAZY (56)	χ_a^2 EAZY (57)	N_{filters} EAZY (58)
9.66	1.77	28.76	1.97	0	-2.05	0	38.00	2.46	0	-2.72	0	-99.00	1.45	5.56	7.19	8
527.06	2.94	313.92	15.44	4	-7.04	1	256.42	12.58	4	-8.89	1	-99.00	0.31	0.40	5.07	9
6.86	1.41	11.00	0.76	4	-2.82	0	8.68	1.44	4	-3.85	0	-99.00	0.89	0.75	3.38	9
-99.00	-99.00	0.38	1.73	4	-165.04	0	0.63	2.16	4	-64.05	0	-99.00	0.38	0.02	0.64	7
-99.00	-99.00	0.99	1.16	0	-2.48	0	0.14	1.23	1	-5.89	0	-99.00	1.27	0.49	0.99	7
4.38	0.86	6.62	1.81	4	-52.62	0	7.15	2.08	4	-18.62	0	-99.00	1.04	1.01	2.98	9
-99.00	-99.00	12.53	2.01	1	-2.08	0	11.24	2.38	4	-2.13	0	-99.00	0.72	0.60	0.62	7
-99.00	-99.00	-0.66	1.26	0	-4.26	0	-1.81	0.93	4	-3.01	0	-99.00	0.36	0.01	5.41	7
-99.00	-99.00	8.06	1.49	0	-2.60	0	5.71	2.05	1	-6.45	0	-99.00	2.07	2.61	1.09	7
2.15	0.58	-1.46	1.88	4	-20.43	0	0.97	1.92	4	-12.40	0	-99.00	0.60	0.27	3.14	8
57.82	3.56	160.17	7.57	0	-12.22	0	105.35	5.08	0	-6.01	0	-99.00	0.11	0.10	843.51	9
5.26	0.75	8.65	1.63	4	-23.95	0	5.08	1.35	0	-21.92	1	-99.00	0.86	0.71	3.80	8
-99.00	-99.00	-0.25	0.18	0	-9.92	0	-2.44	0.36	0	-5.65	2	-99.00	0.81	0.23	7.90	6
-99.00	-99.00	1.19	1.69	0	-2.47	0	1.16	1.96	1	-6.60	0	-99.00	1.50	2.20	2.10	7
31.55	1.40	42.23	2.67	0	-11.98	0	30.66	2.06	0	-6.04	0	-99.00	0.74	0.78	5.03	9
14.44	2.00	16.38	1.90	1	-2.63	0	11.74	1.80	1	-2.24	0	-99.00	0.99	0.97	3.23	8
-99.00	-99.00	0.88	1.70	4	-13.09	0	-0.15	0.01	4	-8.50	2	-99.00	0.49	0.40	1.07	6
-99.00	-99.00	-7.74	2.49	4	-15.10	2	-6.37	1.97	4	-15.97	2	-99.00	3.40	0.42	0.25	5
-99.00	-99.00	11.20	1.44	0	-2.48	0	15.69	1.93	0	-1.97	0	-99.00	2.41	1.71	0.34	7
7.41	1.66	6.22	1.43	0	-7.83	0	6.79	2.23	4	-9.51	0	-99.00	0.41	0.40	5.66	8
1.91	0.52	4.18	1.60	0	-2.05	0	1.47	2.08	1	-2.21	0	-99.00	0.68	0.69	17.49	9
-99.00	-99.00	1.17	1.31	0	-2.36	0	0.88	1.35	0	-1.77	0	-99.00	1.56	2.47	1.85	7
3.24	0.77	7.42	1.78	0	-2.60	0	4.82	1.67	0	-2.56	0	-99.00	0.68	0.75	17.36	9
-99.00	-99.00	-1.00	1.52	4	-7.91	0	-0.45	1.84	4	-3.44	0	-99.00	3.36	4.27	3.28	7
-99.00	-99.00	1.28	1.61	4	-28.68	0	-0.05	0.01	4	-71.67	2	-99.00	2.89	4.11	0.71	6
-99.00	-99.00	0.52	1.50	0	-2.37	0	1.20	1.53	0	-1.76	0	-99.00	1.65	0.26	0.58	7
-99.00	-99.00	4.05	0.19	0	-4.35	0	-0.81	2.11	4	-2.79	0	-99.00	0.80	0.69	2.62	7
-99.00	-99.00	2.48	0.46	1	-3.00	0	2.40	1.74	1	-2.15	0	-99.00	1.01	0.93	0.07	7
-99.00	-99.00	-0.23	1.43	1	-5.42	0	-0.88	1.96	1	-3.41	0	-99.00	1.43	0.07	0.94	7
-99.00	-99.00	5.58	1.68	0	-5.54	0	4.70	1.53	0	-3.29	0	-99.00	1.64	1.52	0.51	7
38.58	1.42	72.10	4.09	1	-4.56	0	63.25	3.88	1	-3.37	0	-99.00	0.99	1.03	5.93	9
37.73	3.57	13.42	2.10	1	-2.41	0	8.60	1.57	0	-2.36	0	-99.00	0.42	0.40	57.04	9
7.63	0.98	6.50	1.87	0	-211.86	0	3.16	1.54	0	-46.32	0	-99.00	0.31	0.22	44.47	9
-99.00	-99.00	-0.30	0.74	0	-4.93	0	-0.79	1.09	1	-3.33	0	-99.00	2.09	0.03	3.84	7
-99.00	-99.00	0.73	0.56	4	-18.94	0	-0.16	0.41	1	-9.67	0	-99.00	1.61	0.07	2.18	7
-99.00	-99.00	5.18	0.98	0	-2.37	0	3.98	1.42	0	-2.68	0	-99.00	0.58	0.13	0.69	7
-99.00	-99.00	4.63	1.83	4	-4159.75	0	3.92	1.44	0	-2565.74	0	-99.00	2.04	2.95	0.65	7
84.25	3.82	44.70	3.32	1	-2.00	0	35.51	3.30	1	-2.09	0	-99.00	0.24	0.23	3.94	9
-99.00	-99.00	0.38	1.58	1	-2.24	0	1.40	1.65	1	-2.27	0	-99.00	0.68	0.76	0.58	7
17.12	0.95	55.59	3.24	1	-14.21	0	36.57	2.75	1	-7.13	0	-99.00	0.05	4.16	146.62	9
-99.00	-99.00	-0.21	0.01	0	-1.81	2	-0.49	0.02	0	-1.77	2	-99.00	1.70	0.42	0.24	5
12.02	1.27	14.08	2.14	1	-2.26	0	15.92	2.35	4	-2.07	0	-99.00	0.96	1.07	4.64	9
84.16	0.96	51.44	2.83	0	-2.67	0	57.48	3.07	0	-2.32	0	-99.00	0.28	0.29	6.85	9
5.48	0.77	7.06	1.50	0	-2.44	0	6.06	1.33	0	-2.22	0	-99.00	0.66	0.68	10.13	9
-99.00	-99.00	1.56	0.09	4	-1.81	0	-0.77	1.04	4	-1.80	0	-99.00	1.91	0.07	3.32	7
4.00	0.77	0.53	1.51	4	-7.20	0	1.02	0.05	4	-8.10	0	-99.00	0.81	0.32	17.95	8

NOTE. — Table 6 is published in its entirety in the machine-readable format. A portion is shown here for guidance regarding its form and content. (1) Unique object ID number, (2) object R.A. (J2000) in decimal degrees, (3) object decl. (J2000) in decimal degrees, (4) semimajor axis in the detection image, (5) ellipticity measured in the detection image, defined as $e = 1 - b/a$, where b and a are the semiminor and semimajor axes, respectively, (6) position angle measured in the detection image (degrees E from N), (7) SExtractor Kron radius used in AUTO photometry, (8) SExtractor half-light radius (FLUX_RADIUS), (9,15,21,27,33) DECam *ugriz* PSF fluxes appropriate for unresolved sources, (10,16,22,28,34) Errors on DECam *ugriz* PSF fluxes, (11,17,23,29,35) DECam *ugriz* total (Kron) fluxes, (12,18,24,30,36) Errors on DECam *ugriz* total fluxes, (13,19,25,31,37) DECam *ugriz* SExtractor internal flags, (14,20,26,32,38) DECam *ugriz* SExtractor external flags, (39) *JK* object ID number from Geach et al. (2017), (40,42) *JK* total (Kron) fluxes, (41,43) Errors on *JK* total fluxes, (44,49) 3.6 and 4.5 μm IRAC Tractor total fluxes, (45,50) 3.6 and 4.5 μm IRAC Tractor errors, (46,51) 3.6 and 4.5 μm IRAC Tractor model profiles, (47,52) 3.6 and 4.5 μm IRAC Tractor log-probabilities, (48,49) 3.6 and 4.5 μm IRAC Tractor flags, (54) SDSS spectroscopic redshift, (55) EAZY peak photometric redshift, (56) EAZY χ^2 minimum photometric redshift, (57) EAZY χ^2 minimum value, (58) EAZY number of filters used in photometric redshift estimate.